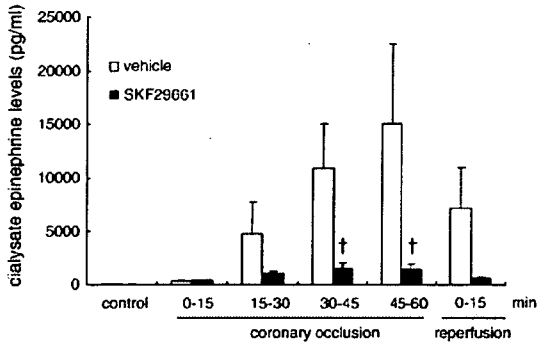

Fig. 2. Time course of dialysate epinephrine levels during coronary occlusion. Values are means±SE. †$P<0.05$ vs. concurrent value of vehicle group.

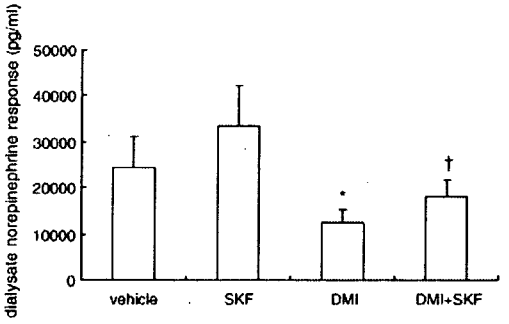

Fig. 4. Dialysate norepinephrine responses to 60 min coronary occlusion. SKF = SKF29661, DMI = desipramine, DMI+SKF = desipramine+SKF29661. Values are means±SE. *$P<0.05$ vs. value of vehicle group. †$P<0.05$ vs. value of SKF group.

3.3. Dialysate EPI levels in the ischemic region

Coronary occlusion significantly increased dialysate EPI levels (Fig. 2). In the vehicle group, dialysate EPI levels were 59.6±39.8 pg/ml in the control and increased after coronary occlusion. During 60 min coronary occlusion, dialysate EPI levels markedly increased and reached 15030±7418 pg/ml ($n=6$) at 45–60 min of occlusion. After reperfusion, dialysate EPI levels decreased to 7193±3722 pg/ml, although their levels were higher than those in the control. In the presence of SKF29661, dialysate EPI levels also increased and reached 1493±196 pg/ml ($n=6$) at 45–60 min of occlusion. These increases in dialysate EPI levels after 30 min of coronary occlusion were significantly attenuated by SKF29661.

3.4. Dialysate EPI levels in the ischemic region during local desipramine administration

Although coronary occlusion increased dialysate EPI levels, these levels were suppressed during local desipramine administration compared to the vehicle group (Fig. 3). During 60 min coronary occlusion, dialysate EPI levels increased and reached 743±171 pg/ml ($n=6$) at 45–60 min of occlusion. After reperfusion, dialysate EPI levels decreased to 400±181 pg/ml, although their levels were higher than those in the control. In the presence of SKF29661, dialysate EPI levels also increased and reached 725±154 pg/ml ($n=6$) at 45–60 min of occlusion. These increases in dialysate EPI levels were not attenuated by SKF29661.

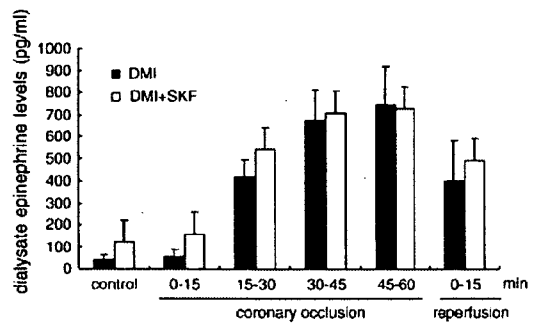

Fig. 3. Influence of desipramine on dialysate EPI levels during myocardial ischemia with and without SKF29661. DMI = desipramine, DMI+SKF = desipramine+SKF29661. Values are means±SE.

3.5. Comparison of peak dialysate NE levels of the 4 groups

EPI is synthesized from NE, and so myocardial interstitial NE levels might affect myocardial interstitial EPI levels. We compared with myocardial interstitial NE levels at 45–60 min of coronary occlusion in the vehicle group, the SKF29661 group, the desipramine group and the desipramine and SKF29661 group (Fig. 4) ($n=6$-6-6-6). In the latter two groups (desipramine, desipramine+SKF29661), ischemia-induced peak dialysate NE levels were significantly suppressed in comparison with that of the vehicle or SKF29661 group. Calculated ratios of interstitial EPI/NE were 1.5±0.4 and 12±4% at NE infusion (250 ng) and 45–60 min of occlusion, respectively.

4. Discussion

4.1. Changes in myocardial interstitial EPI levels during local administration of NE through a dialysis probe

Local administration of NE dose dependently increased dialysate EPI levels. The pretreatment with PNMT inhibitor SKF29661 significantly suppressed these increases. Therefore, the EPI levels in dialysate could serve as an index of PNMT activity during local administration of NE. To our knowledge, this is the first direct assessment of cardiac PNMT activity in in vivo heart. These results indicate that EPI can be regionally synthesized from NE with PNMT activity in the heart. Regionally administered NE in myocardial interstitium was taken up by cardiac sympathetic nerve endings via the uptake$_1$ carrier or by extraneuronal cells via uptake$_2$ carrier [19–21]. Several studies demonstrated the existence of PNMT in the myocardium rather than

sympathetic nerve endings [17,22]. In sympathetic denervation with 6-OHDA, the dialysate EPI response to NE infusion was preserved. The dialysate EPI response was suppressed by pretreatment with corticosterone (an NE $uptake_2$ inhibitor). Our data were also consistent with those studies. NE might be taken up by myocardial cell via $uptake_2$ carrier and converted to EPI with PNMT. Recent study has shown that gene expression of the PNMT is localized not in cardiac ganglion, but in cardiomyocytes [23]. Therefore, our data suggest that high NE level in myocardial interstitium yields EPI synthesis by regional PNMT activity. NE that was taken up by extraneuronal cells was metabolized mainly to normetanephrine (NMN) or 3-methoxy-4-hydroxyphenylglycol (MHPG) by catechol *O*-methyltransferase (COMT) [19], but high NE was partly available for EPI synthesis with PNMT. These elevated NE levels were similar to the levels of myocardial ischemic regions in our previous studies [6,24]. Therefore, EPI synthesis with PNMT may gain relevance during myocardial ischemia.

4.2. Myocardial interstitial EPI levels during coronary artery occlusion

Coronary occlusion-induced progressive increases in dialysate EPI levels. These increases corresponded to increases in dialysate NE levels. Our data suggest that the high NE level evoked by myocardial ischemia yields EPI synthesis by regional PNMT activity. During myocardial ischemia, calculated ratio of interstitial EPI/NE was eight-times higher than that of NE infusion. In the ischemic heart, normal transport of NE is impaired because of a reduced sodium gradient [5], whereas another uptake system is operative by extraneuronal cells via the $uptake_2$ carrier which is independent of the sodium gradient [25]. Actually myocardial ischemia evoked increases in myocardial interstitial NMN or MHPG via the $uptake_2$ carrier [26]. The time course of dialysate EPI levels corresponded to increases in dialysate NE and NMN levels. Therefore, we consider that released NE is taken up by extraneuronal cells and PNMT activity for EPI synthesis is operative at high concentration of NE.

To confirm EPI synthesis via PNMT activity, we examined ischemia-induced dialysate EPI levels in the presence and absence of a PNMT inhibitor. PNMT inhibition suppressed the increase in dialysate EPI (synthesis by PNMT) and augmented the increase in dialysate NE (substrate of PNMT) levels. Thus, in the ischemic period as well as local administration of NE, PNMT activity plays an important physiological role in NE gradation and EPI synthesis. The PNMT activity in the ischemic left ventricle augmented EPI production by excess of substrate. The increased PNMT activity might reflect compensatory or adaptation processes secondary to impairments of the catecholamine uptake system and its degradation via monoamine oxidase [6].

At the myocardial interstitial space, local ω-conotoxin GVIA treatment attenuated the EPI release in response to cardiac sympathetic nerve stimulation [18]. Furthermore, local tyramine administration caused an increase in dialysate EPI level via a non-exocytotic mechanism. The previous study demonstrated that EPI is released from vesicle and axoplasma via exocytosis and carrier-mediated transport in the cardiac sympathetic nerve endings. In the resting state, myocardial interstitial EPI is extracted mainly from circulating EPI and taken up via catecholamine transporter to nerve endings. Therefore, in the sympathetic nerve endings containing EPI, the non-exocytotic release via outward transport would be involved in EPI release evoked by myocardial ischemia.

Myocardial ischemia-induced increases in dialysate EPI levels were suppressed by the pretreatment with desipramine. Desipramine suppressed peak EPI levels by 5% of vehicle group. Marked suppression of EPI release can be explained by two possible mechanisms. First, desipramine inhibits both directions of NE transport through $uptake_1$ carrier [5,27]. Ischemia-induced outward NE transport through $uptake_1$ carrier is inhibited by desipramine, and so myocardial interstitial NE levels are also attenuated [6]. In this way, desipramine reduced the substrate of EPI via PNMT and EPI synthesis in extraneuronal cells. Alternatively, EPI is released via carrier-mediated outward transport of EPI from sympathetic nerve endings. The present study could not clarify whether EPI specific transporter or NE transporter is involved in carrier-mediated outward transport of EPI. But desipramine inhibits transports of both EPI and NE. Thus, both actions of desipramine on NE and EPI caused a marked decrease in the EPI release evoked by myocardial ischemia. Although desipramine markedly suppressed the EPI release evoked by myocardial ischemia, it is uncertain which factor is more responsible for EPI release.

Finally, to elucidate which of these two mechanisms is mainly involved in the EPI release evoked by myocardial ischemia, we compared ischemia-induced EPI release between desipramine alone and the combination of desipramine and SKF29661 pretreatments. Myocardial ischemia-induced EPI release did not differ between the two groups. This result indicates that the EPI synthesis by PNMT might not be involved in the EPI release evoked by myocardial ischemia. In the presence of desipramine, myocardial interstitial NE levels were markedly suppressed. These NE levels might not be operative as the substrate of EPI whereas only the markedly higher NE level in vehicle group might be operative as the substrate of EPI and yield EPI synthesis via PNMT activity. Thus, PNMT in the left ventricle is capable of synthesizing EPI with markedly elevated NE in the myocardial interstitial space. As well as COMT system [28], cardiac PNMT plays an important physiological role in NE degradation during high concentrations of myocardial interstitial NE. Since EPI preferentially interacts with $beta_2$-adrenergic receptors in heart [29]. Regional EPI might promote exocytotic NE release by activating presynaptic $beta_2$-adrenergic receptors. Future work should concentrate on these aspects of cardiac PNMT.

4.3. Methodological considerations

In general, EPI is released from the adrenal medulla and carried to the heart via the bloodstream [9]. In the present study, we administered a PNMT inhibitor SKF29661 intraperitoneally to block EPI synthesis. SKF29661 may inhibit EPI synthesis at the adrenal grand and reduce blood EPI levels. In this way, administration of SKF29661 might affect EPI uptake and the content of EPI at the cardiac sympathetic nerve endings. There was no significant difference in the control dialysate EPI level between vehicle and SKF29661 group. Therefore, we believe that extraction of EPI from plasma EPI does not change the quantitative results obtained from the cardiac dialysis.

Animal studies demonstrated that two enzymes are involved in EPI synthesis: PNMT and nonspecific *N*-methyltransferase [30]. Nonspecific *N*-methyltransferase is less inhibited by the PNMT inhibitor SKF29661. This nonspecific *N*-methyltransferase was reported to be present in the heart, but the predominant cardiac enzyme is apparently PNMT. Actually pretreatment with SKF29661 suppressed NE-induced EPI release by 10% of vehicle group. Therefore, it is thought that nonspecific *N*-methyltransferase exerts little effect on the EPI release evoked by NE administration or myocardial ischemia.

In conclusion, there is a PNMT activity in the heart. Under local administration of NE or ischemic conditions, PNMT in the left ventricle is capable of synthesizing EPI with markedly elevated NE in the myocardial interstitial space. We consider two mechanisms to be involved in the increment of EPI during myocardial ischemia, namely EPI synthesis by cardiac PNMT in extraneuronal cells and the non-exocytotic release from the sympathetic nerve endings.

Acknowledgements

This work was supported by Grants-in-Aid for scientific research (17591659) from the Ministry of Education, Culture, Sports, Science and Technology. The authors thank Glaxosmithkline for the supply of SKF29661.

References

[1] Lameris TW, de Zeeuw S, Alberts G, Boomsma F, Duncker DJ, Verdouw PD, et al. Time course and mechanism of myocardial catecholamine release during transient ischemia in vivo. Circulation 2000;101:2645–50.

[2] Kuroko Y, Fujii T, Yamazaki T, Akiyama T, Ishino K, Sano S, et al. Contribution of catechol *O*-methyltransferase to the removal of accumulated interstitial catecholamines evoked by myocardial ischemia. Neurosci Lett 2005;388:61–4.

[3] Penny WJ. The deleterious effects of myocardial catecholamines on cellular electrophysiology and arrhythmias during ischaemia and reperfusion. Eur Heart J 1984;5:960–73.

[4] Waldenstrom AP, Hjalmarson AC, Thornell L. A possible role of noradrenaline in the development of myocardial infarction: an experimental study in the isolated rat heart. Am Heart J 1978;95: 43–51.

[5] Schömig A, Dart AM, Dietz R, Mayer E, Kubler W. Release of endogenous catecholamines in the ischemic myocardium of the rat. Part A: locally mediated release. Circ Res 1984;55:689–701.

[6] Akiyama T, Yamazaki T. Myocardial interstitial norepinephrine and dihydroxyphenylglycol levels during ischemia and reperfusion. Cardiovasc Res 2001;49:78–85.

[7] Axelrod J. Purification and properties of phenylethanolamine-*N*-methyl transferase. J Biol Chem 1962;237:1657–60.

[8] Peronnet F, Boudreau G, de Champlain J, Nadeau R. Effect of changes in myocardial epinephrine stores on plasma norepinephrine gradient across the dog heart. Am J Physiol 1994;266:H2404–9.

[9] Elayan HH, Kennedy BP, Ziegler MG. Cardiac atria and ventricles contain different inducible adrenaline synthesising enzymes. Cardiovasc Res 1990;24:53–6.

[10] Ziegler MG, Bao X, Kennedy BP, Joyner A, Enns R. Location, development, control, and function of extraadrenal phenylethanolamine *N*-methyltransferase. Ann N Y Acad Sci 2002;971:76–82.

[11] Akiyama T, Yamazaki T, Ninomiya I. Differential regional responses of myocardial interstitial noradrenaline levels to coronary occlusion. Cardiovasc Res 1993;27:817–22.

[12] Yamazaki T, Akiyama T, Kitagawa H, Takauchi Y, Kawada T, Sunagawa K. A new, concise dialysis approach to assessment of cardiac sympathetic nerve terminal abnormalities. Am J Physiol 1997;272:H1182–7.

[13] Akiyama T, Yamazaki T, Ninomiya I. In vivo monitoring of myocardial interstitial norepinephrine by dialysis technique. Am J Physiol 1991;261: H1643–7.

[14] Yamazaki T, Akiyama T, Shindo T. Routine high-performance liquid chromatographic determination of myocardial interstitial norepinephrine. J Chromatogr B Biomed Appl 1995;670:328–31.

[15] Takauchi Y, Kitagawa H, Kawada T, Akiyama T, Yamazaki T. High-performance liquid chromatographic determination of myocardial interstitial dihydroxyphenylglycol. J Chromatogr B Biomed Sci Appl 1997;693:218–21.

[16] Kennedy B, Elayan H, Ziegler MG. Lung epinephrine synthesis. Am J Physiol 1990;258:L227–31.

[17] Tse J, Rodriques E, Gonzalez M, Weiss HR. Effects of chemical denervation with 6-hydroxydopamine on myocardial responsiveness to isoproterenol in rabbits. Basic Res Cardiol 1995;90:380–7.

[18] Kawada T, Yamazaki T, Akiyama T. Local epinephrine release in the rabbit myocardial interstitium in vivo. J Auton Nerv Syst 2000;78: 94–8.

[19] Trendelenburg U. The extraneuronal uptake and metabolism of catecholamines in the heart. In: Paton DM, editor. The mechanism of neuronal and extraneuronal transport of catecholamines. 1st ed. New York: Raven Press; 1976. p. 259–80.

[20] Grohmann M, Trendelenburg U. The substrate specificity of uptake$_2$ in the rat heart. Naunyn Schmiedebergs Arch Pharmacol 1984;328: 164–73.

[21] Obst OO, Rose H, Kammermeier H. Characterization of catecholamine uptake$_2$ in isolated cardiac myocytes. Mol Cell Biochem 1996;163–164: 181–3.

[22] Torda T, Culman J, Petrikova M. Distribution of phenylethanolamine-*N*-methyltransferase in the rat heart: effect of 6-hydroxydopamine. Eur J Pharmacol 1987;141:305–8.

[23] Krizanova O, Micutkova L, Jelokova J, Filipenko M, Sabban E, Kvetnansky R. Existence of cardiac PNMT m-RNA in adult rats: elevation by stress in a glucocorticoid-dependent manner. Am J Physiol Heart Circ Physiol 2001;281:H1372–9.

[24] Shindo T, Akiyama T, Yamazaki T, Ninomiya I. Regional myocardial interstitial norepinephrine kinetics during coronary occlusion and reperfusion. Am J Physiol 1996;270:H245–51.

[25] Schömig E, Russ H, Staudt K, Martel F, Gliese M, Gründemann. The extraneuronal monoamine transporter exists in human central nervous system glia. Adv Pharmacol 1998;42:356–9.

[26] Fujii T, Yamazaki T, Akiyama T, Sano S, Mori H. Extra neuronal enzymatic degradation of myocardial norepinephrine in the ischemic region. Cardiovasc Res 2004;64:125–31.

[27] Schömig A, Fischer S, Kurz T, Richardt G, Schomig E. Nonexocytotic release of endogenous noradrenaline in during in the ischemic and anoxic rat heart: mechanism and metabolic requirements. Circ Res 1987;60:194–205.
[28] Carlsson L, Graefe KH, Trendelenburg U. Early intraneuronal mobilization and deamination of noradrenaline during global ischemia in the isolated perfused rat heart. Naunyn Schmiedebergs Arch Pharmacol 1987;336:508–18.
[29] Lands AM, Arnold A, McAuliff JP, Luduena FP, Brown Jr TG. Differentiation of receptor systems activated by sympathumimetic amines. Nature 1967;214:597–8.
[30] Zeigler MG, Kennedy B, Elayan H. Extraadrenal adrenaline formation by two separate enzymes. Experintia 1989;45:718–20.

ORIGINAL RESEARCH

K. Myojin
A. Taguchi
K. Umetani
K. Fukushima
N. Nishiura
T. Matsuyama
H. Kimura
D.M. Stern
Y. Imai
H. Mori

Visualization of Intracerebral Arteries by Synchrotron Radiation Microangiography

BACKGROUND AND PURPOSE: Small cerebral vessels are a major site for vascular pathology leading to cerebral infarction and hemorrhage. However, such small cerebral vessels are difficult to visualize by using conventional methods. The goal of our study was the development of methodology allowing visualization of small cerebral arteries in rodents, suitable for experimental models.

MATERIALS AND METHODS: Using barium sulfate as a contrast material, we obtained microangiographic images of physiologic and pathologic changes consequent to cerebral infarction in mouse brain by monochromatic synchrotron radiation (SR). To achieve high-resolution and high-contrast images, we used a new x-ray camera with a pixel size of 4.5 μm, and we set the energy level at 37.5 keV, just above the K absorption of barium.

RESULTS: Small intracerebral arteries (~30 μm in diameter) were clearly visualized, as well as the cortical branches (50–70 μm in diameter) at the brain surface. The limit of detection appeared to be vessels ~10 μm in diameter. Compared with the noninfarcted side, the number of intracerebral arteries was dramatically decreased in the middle cerebral artery area affected by stroke.

CONCLUSIONS: These results indicate the potential of SR for evaluating pathologic changes in small cerebral arteries and for monitoring the impact of pro- and antiangiogenic therapeutic strategies.

Cerebrovascular disease is one of the major causes of death and disability in developed countries. To evaluate cerebral vasculature, conventional angiography and MR angiography are commonly used in clinical practice. The development of these imaging methods has allowed analysis of the pathologic features of cerebrovascular lesions and has guided therapeutic strategies. However, small cerebral vessels, including those known to harbor causative lesions in cerebral infarction and hemorrhage (due to lipohyalinotic changes and/or microaneurysm formation),[1] such as intracerebral arteries and perforators, are below the detection limit of conventional imaging techniques. An important step in developing therapeutic strategies effective against disease in small cerebral vessels is enhanced visualization of this vasculature, especially in experimental models.

Recently, ex vivo and in vivo microangiography using monochromatic synchrotron radiation (SR) has been suggested as a tool capable of visualizing pathophysiologic changes in small arteries. Using this system has made possible the detection of microcirculation in the dermis,[2] tumors,[3] and collateral microvessels in ischemic hind limbs.[4] Although fluorescence microscopy has also been used to image small arteries,[5–7] SR imaging has the advantage of visualizing microvessels, even after they enter the parenchyma of an organ. In contrast, fluorescence techniques do not allow adequate visualization of small arteries once a vessel is deep within brain or other parenchymal tissue. On the basis of these observations, we have developed a microangiographic system using SR and have investigated physiologic and pathologic features of rodent cerebral microvasculature.

Received August 3, 2006; accepted after revision August 31.

From the Departments of Cerebrovascular Disease (K.M., A.T.) and Cardiac Physiology (K.F., N.N., H.M.), National Cardiovascular Center, Osaka, Japan; the Department of Radiology (K.M., Y.I.), Tokai University School of Medicine, Kanagawa, Japan; Japan Synchrotron Radiation Research Institute (K.U.), Hyogo, Japan; the Department of Internal Medicine (T.M.), Hyogo College of Medicine, Hyogo, Japan; Dainippon Sumitomo Pharma Co Ltd (H.K.), Osaka, Japan; and the Dean's Office (D.M.S.), College of Medicine, Cincinnati University, Cincinnati, Ohio.

Experiments were performed at the SPring-8 BL28B2 beamline with the approval of the Japan Synchrotron Radiation Research Institute (acceptance No. 2005B0358).

This work was partially supported by a Grant-in-Aid for Scientific Research from the Ministry of Health, Labor and Welfare and The New Energy and Industrial Technology Development Organization.

Please address correspondence to Akihiko Taguchi, MD, Department of Cerebrovascular Disease, National Cardiovascular Center, 5-7-1 Fujishiro-dai, Suita, Osaka, Japan, 565-8565; e-mail: Taguchi ataguchi@res.ncvc.go.jp

Materials and Methods

All procedures were performed in accordance with the National Cardiovascular Center Animal Care and Use Committee.

Preparation of Contrast Medium

For high-contrast images of the microcirculation, contrast agents included microspheres (Techpolymer I-2, Sekisui Plastics, Shiga, Japan) and barium sulfate (BarytgenSol, Fushimi, Tokushima, Japan). However, because the diameter of microspheres was 15 μm, whereas that of barium sulfate particles varied from 1–100 μm, the microcirculation of cerebral arteries could not be visualized by using these contrast media (not shown). To perfuse such microvessels (diameter <10 μm), we filtered barium sulfate (pore size 5 μm; Millex-SV, Millipore, Bedford, Mass) and obtained particles <5 μm in diameter. Filtered barium sulfate particles were then centrifuged (3000 G, 60 minutes) and concentrated to 50% by weight following removal of the supernatant.

Injection of Contrast Medium

Male severe combined immunodeficient (SCID) mice (6 weeks old; weight, 25–30 g; Oriental Yeast, Tokyo, Japan) were anesthetized by using inhaled diethyl ether and were perfused systemically with phosphate-buffered saline (PBS) containing heparin (40 U/mL) via the left ventricle of the heart with a peristaltic pump (Iwaki, Asahi Techno Glass, Chiba, Japan). Filtered barium sulfate particles (<5 μm in diameter, prepared as described previously; 50% by weight) were infused (0.7 mL), followed by isolation of the brain and fixation in formalin.

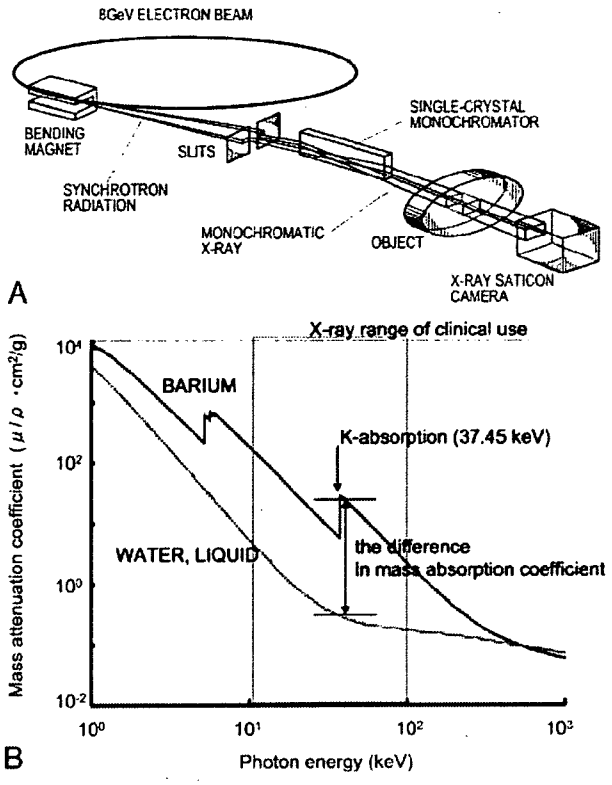

Fig 1. Schematic depiction of the monochromatic SR system. *A*, Illustration of the experimental arrangement for SR microangiography at BL28B2. *B*, Photon mass attenuation coefficient of barium (*blue line*) and liquid water (*red line*). Monochromatic x-ray energy is adjusted to 37.5 keV, just above the barium K-edge energy to produce the highest contrast image.

Microangiography and Image Analysis

Microangiographic images of mouse brain were obtained by using monochromatic SR in the Japan Synchrotron Radiation Research Institute (SPring-8, Hyogo, Japan).[4,8] There are 3 large 3rd-generation synchrotron radiation facilities in the world: the Advanced Photon Source in Argonne (United States), the European Synchrotron Radiation Facility in Grenoble (France), and SPring-8 (the latter was used for the studies described herein). These facilities are open to scientists in many fields, including material, chemical, and life sciences investigators. The experimental setup for x-ray imaging by using monochromatic SR at the SPring-8 BL28B2 beamline is shown in Fig 1*A*. The storage ring was operated at 8-GeV electron beam energy, and beam current was 80–100 mA. The distance between the point source in the bending magnet and the detector was ~45 m. A nearly parallel x-ray beam was used for imaging without blurring because of the small size of the x-ray source and the very long source-to-object distance. The single crystal monochromator selects a single energy of synchrotron radiation. The shutter system is located between the monochromator and the object. X-rays transmitted through the object are detected by an x-ray direct-conversion-type detector incorporating the x-ray saticon pickup tube. Monochromatic x-ray energy was adjusted to 37.5 keV, just above the barium K-edge energy, to produce the highest contrast image of the barium (Fig 1*B*). X-ray flux at the object position was around 1×10^{10} photons/mm^2 per second in imaging experiments. The images were acquired as 1024 × 1024 pixels with 10-bit resolution after analog-to-digital conversion. The FOV was 4.5 × 4.5 mm^2, and pixel size was ~4.5 μm.[9,10]

Mammographic Images

To compare spatial and contrast resolution, we obtained mammographic images, which are known for having the highest resolution in clinical applications,[11] of murine brains. Digital images were captured at an energy level of 24 kV by using a molybdenum target and a molybdenum filter with 90° cranial projection. Source-to-image distance was 65 cm.

Induction of Focal Cerebral Ischemia

Permanent focal cerebral infarction was induced by ligation and disconnection of the left MCA of male SCID mice (n = 5), as described.[12-14] Briefly, under inhaled halothane (3%) anesthesia, animals were placed on their right sides and a skin incision was made at the midpoint between the left orbit and the external auditory canal. The temporalis muscle was incised, and the zygomatic arch was removed to expose the squamous portion of the temporal bone. Using a dental drill, we made a small hole above the distal portion, M1, of the MCA, which could be seen through the exposure in the skull. The dura mater was opened, and the left MCA was electrocauterized and disconnected just distal to its crossing of the olfactory tract. Body temperature was maintained at 36.5°–37°C by using a heat lamp during the operation and for 2 hours after MCA occlusion. Cerebral blood flow (CBF) in the left MCA area was measured by laser-Doppler flowmetry (Advance, Tokyo, Japan). The holding device of the laser probe (ALF probe; Neuroscience, Osaka, Japan) (1.5 mm in diameter, 7.0 mm in length) was secured on the cranium at a site located above the ischemic core of the left MCA area (approximately 1 mm anterior and 5 mm distal to the bregma), and CBF was monitored during the procedure and 24 hours after ligation of the MCA. Mice displaying a decrease in CBF by ~75% immediately after the procedure and thereafter for an additional 24 hours were used for experiments.[15] Nine days after induction of cerebral ischemia, the cerebral microcirculation was examined by SR imaging.

MR Imaging System

To confirm cerebral infarction consequent to ligation of the MCA, we performed MR imaging on day 2 poststroke. MR imaging used a 2T compact MR imaging system with a permanent magnet (MRmini SA206, Dainippon Sumitomo Pharma, Osaka, Japan) by using a radio-frequency solenoid coil for signal-intensity detection. For each imaging sequence, 15 coronal images were acquired with a section thickness of 1 mm, gapped at 0.5 mm. T1-weighted spin-echo MR images were acquired with a TR/TE of 500/9 ms, a FOV of 36.6 × 18.3 mm, an image acquisition matrix of 256 × 128, and NEX, 4. T2-weighted spin-echo MR images were obtained with TR/TE, 3000/69, 256 × 128, and NEX, 2. Because the sequences to obtain diffusion-weighted images by using this machine are still in development, we evaluated the cerebral ischemia by T2-weighted images on day 2 poststroke.

Data Analysis

In all experiments, the mean ± SE is reported.

Results

Visualization of Cerebral Arteries by SR Imaging

After euthanasia and systemic perfusion with PBS, barium sulfate particles were infused via the left ventricle of the heart. As shown in Fig 2*A*, cerebral arteries on the brain surface were filled with contrast medium. First, we investigated vascular

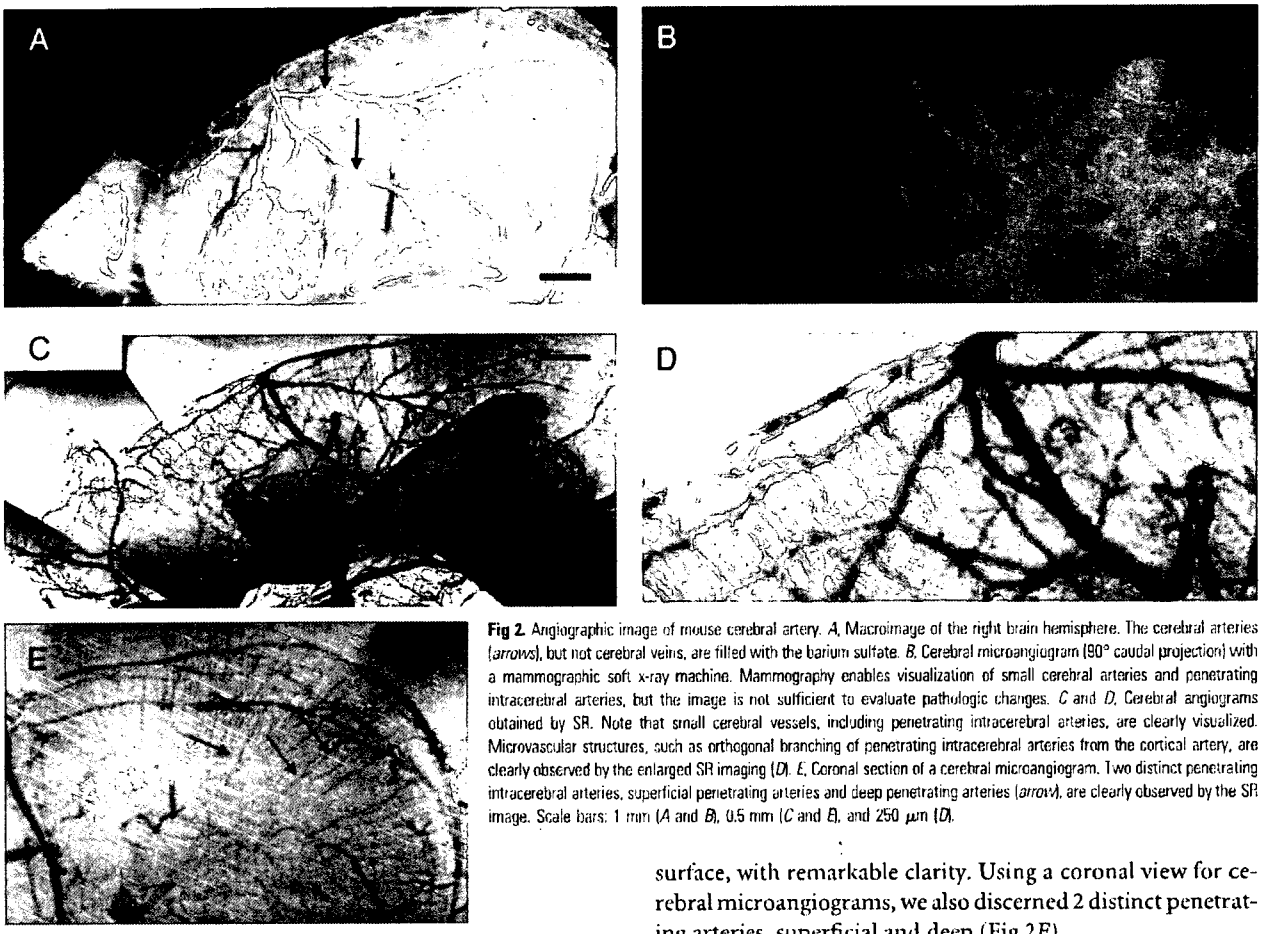

Fig 2. Angiographic image of mouse cerebral artery. *A*, Macroimage of the right brain hemisphere. The cerebral arteries (*arrows*), but not cerebral veins, are filled with the barium sulfate. *B*, Cerebral microangiogram (90° caudal projection) with a mammographic soft x-ray machine. Mammography enables visualization of small cerebral arteries and penetrating intracerebral arteries, but the image is not sufficient to evaluate pathologic changes. *C* and *D*, Cerebral angiograms obtained by SR. Note that small cerebral vessels, including penetrating intracerebral arteries, are clearly visualized. Microvascular structures, such as orthogonal branching of penetrating intracerebral arteries from the cortical artery, are clearly observed by the enlarged SR imaging (*D*). *E*, Coronal section of a cerebral microangiogram. Two distinct penetrating intracerebral arteries, superficial penetrating arteries and deep penetrating arteries (*arrow*), are clearly observed by the SR image. Scale bars: 1 mm (*A* and *B*), 0.5 mm (*C* and *E*), and 250 μm (*D*).

images by mammography (Fig 2*B*). However, sufficient spatial and contrast resolution was not obtained by mammographic imaging to evaluate the angioarchitecture of small cerebral vasculature. Peripheral branches of the MCA (75–100 μm in diameter) and small vessels emerging from peripheral branches were barely visualized.

Next, we investigated the vascular profile by using SR (Fig 2*C*, normal view; -*D*, enlarged view). At the brain surface, cortical arteries branching from the MCA and pial arteries, ~30 μm in diameter, were clearly visualized. Within the brain parenchyma, penetrating intracerebral arteries, branching orthogonally from cortical or pial arteries, were also observed. The interval between intracerebral arteries was 126.1 ± 35.5 μm (n = 20), the diameter of the proximal side of the intracerebral arteries was 29.5 ± 3.1 μm (n = 20), and each intracerebral artery was observed to progressively narrow to a diameter below the limit of resolution (10 μm). Vascular diameters determined by SR imaging of intracerebral arteries and small arterial branches were identical to those observed in previous pathologic studies of murine brain.[16] Using SR imaging, we could discern 2 types of intracerebral arteries: superficial penetrating arteries perfusing only the cortical area and penetrating arteries reaching the subcortical area and perfusing the deep white matter. These vascular structures observed in murine brain by SR imaging are similar to previous observations in human anatomic studies.[17-20] Compared with mammographic images, SR imaging enabled visualization of penetrating intracerebral arteries (diameter range of 10–30 μm), as well as small peripheral branches of MCA at the brain surface, with remarkable clarity. Using a coronal view for cerebral microangiograms, we also discerned 2 distinct penetrating arteries, superficial and deep (Fig 2*E*).

SR Images after Cerebral Infarction

To evaluate cerebral vasculature in the context of pathologic changes, cerebral infarction was induced by ligation of the MCA. The area of cerebral infarction was visualized by MR imaging on day 2 after induction of stroke. As we have shown previously by 2,3,5-triphenyltetrazolium staining,[12] limited cortical infarction was observed in the MCA area on T2-weighted images (Fig 3*A*). In contrast, no hyper- or hypointense region was observed on T1-weighted images (Fig 3*B*), indicating the absence of bleeding or parenchymal injury. Although no morphologic (Fig 3*C*) or vascular structural (Fig 3*D*) changes were observed in the right hemisphere (nonstroke side), by day 9 after MCA occlusion, tissue degradative changes were observed in the cortical and shallow white matter of the left MCA area (stroke side, Fig 3*E*). To evaluate the integrity of the microvasculature after stroke, we obtained SR images. The number of penetrating intracerebral arteries dramatically decreased, though cortical branches at the brain surface could still be visualized (Fig 3*F*). On the coronal view, the disappearance of the intracerebral arteries on the ischemic side was also clearly observed (Fig 3*G*).

Discussion

Cerebral artery disease in small vessels is a major cause of cerebral infarction and hemorrhage. Although pathologic changes in small arteries have been reported on the basis of microscopic analysis, it has been difficult to assess the mor-

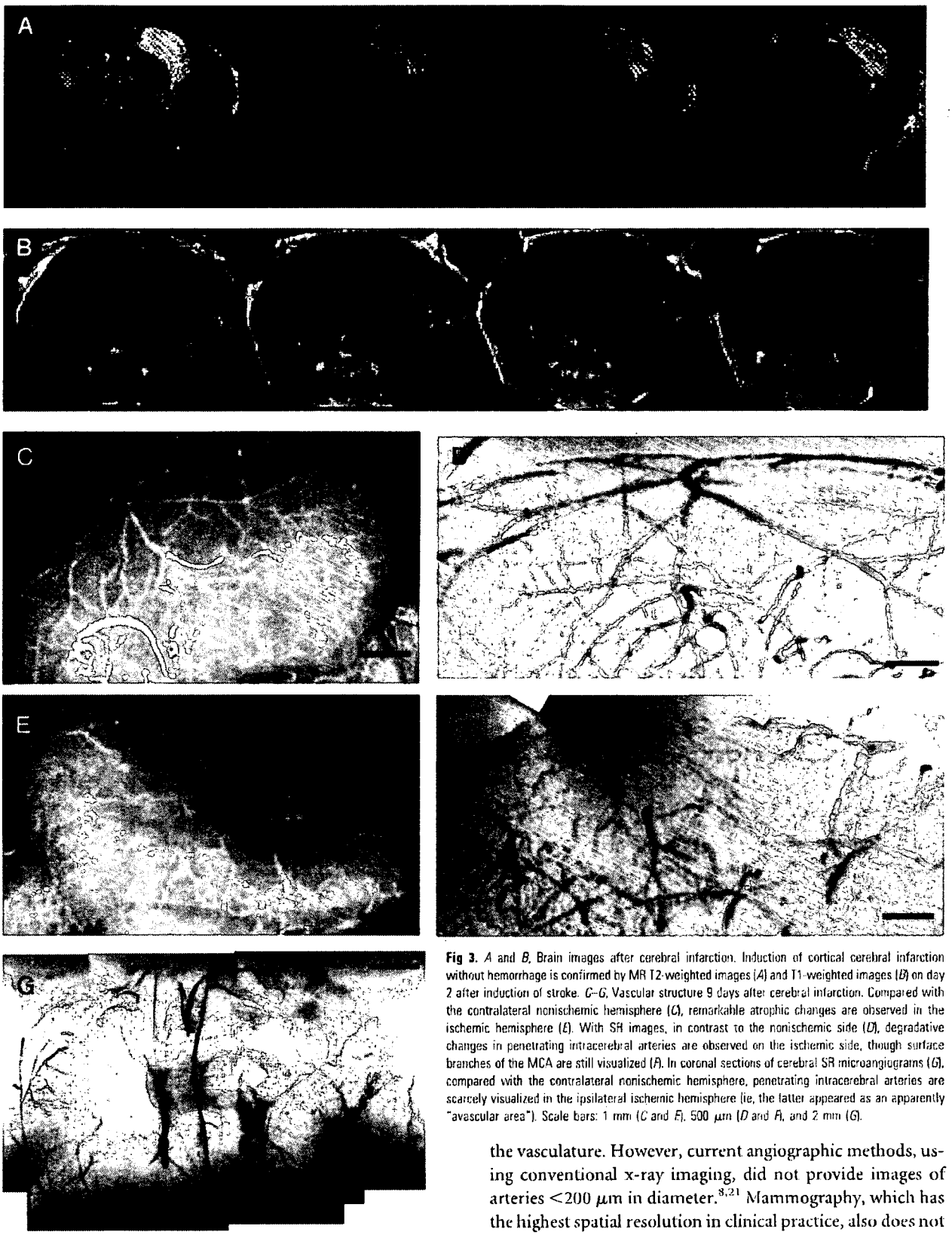

Fig 3. *A* and *B*, Brain images after cerebral infarction. Induction of cortical cerebral infarction without hemorrhage is confirmed by MR T2-weighted images (*A*) and T1-weighted images (*B*) on day 2 after induction of stroke. *C–G*, Vascular structure 9 days after cerebral infarction. Compared with the contralateral nonischemic hemisphere (*C*), remarkable atrophic changes are observed in the ischemic hemisphere (*E*). With SR images, in contrast to the nonischemic side (*D*), degradative changes in penetrating intracerebral arteries are observed on the ischemic side, though surface branches of the MCA are still visualized (*F*). In coronal sections of cerebral SR microangiograms (*G*), compared with the contralateral nonischemic hemisphere, penetrating intracerebral arteries are scarcely visualized in the ipsilateral ischemic hemisphere (ie, the latter appeared as an apparently "avascular area"). Scale bars: 1 mm (*C* and *E*), 500 μm (*D* and *F*), and 2 mm (*G*).

phology of small cerebral vessels in situ through imaging studies. Herein, we demonstrate that small cerebral vessels can be clearly visualized by microangiography by using SR.

Conventional angiography is commonly used to evaluate the vasculature. However, current angiographic methods, using conventional x-ray imaging, did not provide images of arteries <200 μm in diameter.[8,21] Mammography, which has the highest spatial resolution in clinical practice, also does not have sufficient resolution to visualize small vessels with a diameter of <50 μm.[11] Microangiographic techniques have been developed by using fine-focus x-rays and sensitive films to evaluate the microcirculation in the brain.[20] These methods enable visualization of human cortical perforating arteries and

medullary long branches (100 μm in diameter) by using 1-cm-thick sections of brain.[20] However, the limit of detection by using these methods applied to thick sections has been reported to be vessels of 50 μm in diameter.[22] Furthermore, visualization of smaller arteries required thin sections cut with a microtome.[20] The latter method is not well-suited to the evaluation of 3D cerebral vascular trees.

Compared with these conventional methods, the principal advantage of SR is the small size of the electron beam, thereby providing a high-intensity x-ray point source. Using a nearly parallel beam of SR, along with a precise detection system (pixel size of 4.5 μm), allowed us to obtain high-quality angiographic images with excellent spatial resolution. Furthermore, setting SR at an energy level just above the K absorption of barium produced the highest contrast images. SR imaging provides a powerful tool to reveal the morphology of small cerebral arteries such as superficial and deep penetrating arteries, allowing analysis of their physiologic and pathologic properties under a variety of conditions (ie, borderzone in infarction[23,24] and microaneurysm formation).

Fluorescence microscopy is another tool potentially useful for analysis of the microcirculation.[25] Although fluorescence microscopy provides visualization of microcirculation at the brain surface, the advantage of SR imaging is visualization of small vessels that have penetrated into the brain parenchyma, such as the subcortex. In addition, SR imaging allows performance of microangiography with an optimal projection. When the latter is combined with a microinjector, sequential real-time images can be obtained, providing the substrate for hemodynamic analysis.

In this article, we investigated SR imaging after stroke and showed that the SR image reflects pathologic changes previously observed by using anatomic/microscopic analysis. On day 9 after MCA occlusion, arteries on the surface of the cerebrum were visualized by SR, though penetrating intracerebral arteries were not detected. Previous studies have shown that the integrity of the distal cortical artery is usually maintained after occlusion of the proximal artery and that collateral flow is established through expansion of previously existing and/or formation of new vascular channels.[25,26] Analysis with enhanced MR imaging has shown cerebral parenchymal enhancement in the stroke area by 1 week after cerebral infarction,[27] indicative of blood flow in the peri-ischemic area. In contrast, penetrating intracerebral arteries were dramatically decreased in number in the ischemic hemisphere, though cortical branches on the brain surface were maintained after MCA occlusion. It has previously been shown that microvasculature in the ischemic territory displays adhesion of polymorphonuclear leukocytes in postcapillary venules, followed by the disruption of the microvascular network.[28] These previous findings are consistent with the results of our vascular images obtained by SR after ligation of the MCA.

Conclusion

Our study demonstrates, for the first time, the morphologic features of small vascular networks in murine brain by microangiography by using SR imaging. Our approach provides a powerful tool for evaluating potential angiogenic/antiangiogenic therapeutic strategies, as well as pathologic examination of the cerebral microarterial tree.

Acknowledgments

We thank Y. Kasahara, K. Tomiyasu, and M. Aoki for technical assistance.

References

1. Phillips SJ, Whisnant JP. **Hypertension and the brain: The National High Blood Pressure Education Program.** *Arch Intern Med* 1992;152:938–45
2. Ito K, Tanaka E, Mori H, et al. **A microangiographic technique using synchrotron radiation to visualize dermal circulation in vivo.** *Plast Reconstr Surg* 1998;102:1128–33
3. Tokiya R, Umetani K, Imai S, et al. **Observation of microvasculatures in athymic nude rat transplanted tumor using synchrotron radiation microangiography system.** *Academic Radiology* 2004;9:1039–46
4. Takeshita S, Isshiki T, Mori H, et al. **Use of synchrotron radiation microangiography to assess development of small collateral arteries in a rat model of hindlimb ischemia.** *Circulation* 1997;95:805–08
5. Conway JG, Popp JA, Thurman RG. **Microcirculation in periportal and pericentral regions of lobule in perfused rat liver.** *Am J Physiol* 1985;249:G449–56
6. Stock RJ, Cilento EV, McCuskey RS. **A quantitative study of fluorescein isothiocyanate-dextran transport in the microcirculation of the isolated perfused rat liver.** *Hepatology* 1989;9:75–82
7. Birngruber R, Schmidt-Erfurth U, Teschner S, et al. **Confocal laser scanning fluorescence topography: a new method for three-dimensional functional imaging of vascular structures.** *Graefes Arch Clin Exp Ophthalmol* 2000;238:559–65
8. Mori H, Hyodo K, Tanaka E, et al. **Small-vessel radiography in situ with monochromatic synchrotron radiation.** *Radiology* 1996;201:173–77
9. Umetani K, Yagi N, Suzuki Y, et al. **Observation and analysis of microcirculation using high-spatial-resolution image detectors and synchrotron radiation.** *Proceeding of SPIE* 2000;3977:522–33
10. Yamashita T, Kawashima S, Ozaki M, et al. **Images in cardiovascular medicine: mouse coronary angiograph using synchrotron radiation microangiography.** *Circulation* 2002;105:E3–4
11. Kuzmiak CM, Pisano ED, Cole EB, et al. **Comparison of full-field digital mammography to screen-film mammography with respect to contrast and spatial resolution in tissue equivalent breast phantoms.** *Med Phys* 2005;32:3144–50
12. Taguchi A, Soma T, Tanaka H, et al. **Administration of CD34+ cells after stroke enhances neurogenesis via angiogenesis in a mouse model.** *J Clin Invest* 2004;114:330–38
13. Furuya K, Kawahara N, Kawai K, et al. **Proximal occlusion of the middle cerebral artery in C57Black6 mice: relationship of patency of the posterior communicating artery, infarct evolution, and animal survival.** *J Neurosurg* 2004;100:97–105
14. Kitagawa K, Matsumoto M, Mabuchi T, et al. **Deficiency of intercellular adhesion molecule 1 attenuates microcirculatory disturbance and infarction size in focal cerebral ischemia.** *J Cereb Blood Flow Metab* 1998;18:1336–45
15. Matsushita K, Matsuyama T, Nishimura H, et al. **Marked, sustained expression of a novel 150-kDa oxygen-regulated stress protein, in severely ischemic mouse neurons.** *Brain Res Mol Brain Res* 1998;60:98–106
16. Coyne EF, Ngai AC, Meno JR, et al. **Methods for isolation and characterization of intracerebral arterioles in the C57/BL6 wild-type mouse.** *J Neurosci Methods* 2002;120:145–53
17. Herman LH, Ostrowski AZ, Gurdjian ES. **Perforating branches of the middle cerebral artery: an anatomical study.** *Arch Neurol* 1963;8:32–34
18. Kaplan HA. **The lateral perforating branches of the anterior and middle cerebral arteries.** *J Neurosurg* 1965;23:305–10
19. de Reuck J. **The area of the deep perforating branches of the median cerebral artery in man** [in French]. *Acta Anat (Basel)* 1969;74:30–35
20. Salamon G, Combalbert A, Faure J, et al. **Microradiographic study of the arterial circulation of the brain.** *Prog Brain Res* 1968;30:33–41
21. Mori H, Hyodo K, Tubita K, et al. **Visualization of penetrating transmural arteries in situ by monochromatic synchrotron radiation.** *Circulation* 1994;89:863–71
22. Salamon G, Raybaud C, Michotey P, et al. **Angiographic study of cerebral convolutions and their area of vascularization** [in French]. *Rev Neurol (Paris)* 1975;131:259–84
23. Bogousslavsky J, Regli F. **Centrum ovale infarcts: subcortical infarction in the superficial territory of the middle cerebral artery.** *Neurology* 1992;42:1992–98
24. Donnan GA, Norrving B, Bamford JM, et al. **Subcortical infarctions: classification and terminology.** *Cerebrovasc Dis* 1993;3:248–51
25. Tomita Y, Kubis N, Calando Y, et al. **Long-term in vivo investigation of mouse cerebral microcirculation by fluorescence confocal microscopy in the area of focal ischemia.** *J Cereb Blood Flow Metab* 2005;25:858–67
26. Zulch KJ. *Cerebral Circulation and Stroke*. Berlin, Germany: Springer-Verlag; 1971:116
27. Merten CL, Knitelius HO, Assheuer J, et al. **MRI of acute cerebral infarcts: increased contrast enhancement with continuous infusion of gadolinium.** *Neuroradiology* 1999;41:242–48
28. del Zoppo GJ, Mabuchi T. **Cerebral microvessel responses to focal ischemia.** *J Cereb Blood Flow Metab* 2003;23:879–94

Single Injection of a Sustained-release Prostacyclin Analog Improves Pulmonary Hypertension in Rats

Hiroaki Obata[1,2], Yoshiki Sakai[3], Shunsuke Ohnishi[1], Satoshi Takeshita[4], Hidezo Mori[5], Makoto Kodama[2], Kenji Kangawa[6], Yoshifusa Aizawa[2], and Noritoshi Nagaya[1,4]

[1]Department of Regenerative Medicine and Tissue Engineering, National Cardiovascular Center Research Institute, Osaka, Japan; [2]Division of Cardiology, Niigata University Graduate School of Medical and Dental Science, Niigata, Japan; [3]Ono Pharmaceutical Co. Ltd., Research Headquarters, Osaka, Japan; [4]Department of Internal Medicine, National Cardiovascular Center, Osaka, Japan; [5]Department of Cardiac Physiology, National Cardiovascular Center Research Institute, Osaka, Japan; and [6]Department of Biochemistry, National Cardiovascular Center Research Institute, Osaka, Japan

Rationale: Although prostacyclin is recognized as a therapeutic breakthrough for pulmonary hypertension, it needs continuous infusion because of its short action. Therefore, we developed a new drug delivery system for prostacyclin. We prepared ONO-1301MS, a novel sustained-release prostacyclin analog polymerized with poly(D, L-lactic-co-glycolic acid) (PLGA) microspheres.

Objectives: We examined whether ONO-1301MS attenuates monocrotaline (MCT)-induced pulmonary hypertension in rats, and attempted to elucidate the underlying mechanisms responsible for the beneficial effects of ONO-1301MS.

Methods: After MCT injection, rats were randomized to receive a single subcutaneous injection of 100 mg/kg ONO-1301MS or vehicle.

Measurements and Main Results: We prepared ONO-1301MS, which was polymerized with PLGA to release ONO-1301 for 3 weeks. A single administration of ONO-1301MS achieved sustained elevation of its circulating level and plasma cyclic adenosine 3',5'-monophosphate level for 3 weeks, and attenuated an increase in a metabolite of thromboxane A_2 level. Rats had developed pulmonary hypertension 3 weeks after MCT injection; however, treatment with ONO-1301MS significantly attenuated the increases in right ventricular systolic pressure and right ventricular weight to body weight ratio. ONO-1301MS significantly inhibited hypertrophy of pulmonary arteries. Phosphorylation of extracellular signal-regulated protein kinase (ERK) in the lung was significantly increased in the control group, whereas this increase was markedly attenuated by treatment.

Conclusions: We developed a new drug delivery system for prostacyclin using PLGA and ONO-1301. A single injection of ONO-1301MS resulted in sustained activity for 3 weeks, and attenuated pulmonary hypertension, partly through its antiproliferative effect on vascular smooth muscle cells via inhibition of ERK phosphorylation.

Keywords: pulmonary hypertension; prostacyclin analog; sustained-release preparation; extracellular signal regulated kinase; poly(lactic-co-glycolic acid)

AT A GLANCE COMMENTARY

Scientific Knowledge on the Subject

Although prostacyclin is recognized as a therapeutic breakthrough for pulmonary hypertension, it needs continuous infusion because of its short action. For patients with pulmonary hypertension, development of a sustained-release prostacyclin would be beneficial in terms of stable hemodynamics and quality of life.

What This Study Adds to the Field

A single injection of ONO-1301MS resulted in sustained activity for 3 weeks, and attenuated pulmonary hypertension in rats.

Pulmonary arterial hypertension is a rare but life-threatening disease characterized by progressive pulmonary hypertension that leads to right ventricular (RV) failure and death (1). Prostacyclin, a metabolite of arachidonic acid, has vasoprotective effects, including vasodilation, antiplatelet aggregation, and inhibition of smooth muscle cell (SMC) proliferation (2–4). Thus, continuous intravenous infusion of prostacyclin (epoprostenol) has become recognized as a therapeutic breakthrough for pulmonary arterial hypertension (5–7). The dramatic success of long-term intravenous prostacyclin has led to the development of prostacyclin analogs (8–11). Nevertheless, treatment with prostacyclin or its analogs has some problems in the clinical setting. Epoprostenol therapy requires a continuous intravenous infusion device, and is therefore more invasive and uncomfortable than taking prostacyclin analogs. On the other hand, prostacyclin analogs, such as subcutaneously infused treprostinil, inhaled iloprost, and oral beraprost, need continuous infusion or frequent administration because of their short duration of action (5–11). In fact, epoprostenol has a very short half-life (<6 min) (12), treprostinil has been reported to have a half-life of 4.6 hours after cessation of continuous subcutaneous infusion (13), iloprost has a serum half-life of 20 to 25 minutes, and the elimination half-life of beraprost is 35 to 40 minutes after oral administration (12).

Recently, we developed a new type of prostacyclin agonist, ONO-1301 (Figure 1), which has long-lasting prostacyclin activity and an inhibitory effect on thromboxane synthase (14). ONO-1301 does not contain prostanoid structures, such as a five-membered ring or allylic alcohol, which are digested by 15-hydroxyprostaglandin dehydrogenase (Figure 1). These structures are considered to be crucial for the stable activity of ONO-1301. This agent is metabolized by cytochrome P450, and the half-life was about 5.6 hours in our previous study (14). In

(*Received in original form March 1, 2007; accepted in final form October 26, 2007*)

Supported by research grants from Ono Pharmaceutical Co., Ltd. (no. 526); Human Genome Tissue Engineering 009 from the Ministry of Health, Labor, and Welfare; the Program for Promotion of Fundamental Studies in Health Science of the National Institute of Biomedical Innovation (NIBIO); and a Grant-in-Aid for Exploratory Research from the Ministry of Education, Culture, Sports, Science, and Technology.

Correspondence and requests for reprints should be addressed to Noritoshi Nagaya, M.D., Department of Regenerative Medicine and Tissue Engineering, National Cardiovascular Center Research Institute, 5-7-1 Fujishirodai, Suita, Osaka 565-8565, Japan. E-mail: nnagaya@ri.ncvc.go.jp

This article contains an online supplement, which is accessible from this issue's table of contents at www.atsjournals.org

Am J Respir Crit Care Med Vol 177. pp 195–201, 2008
Originally Published in Press as DOI: 10.1164/rccm.200703-349OC on November 1, 2007
Internet address: www.atsjournals.org

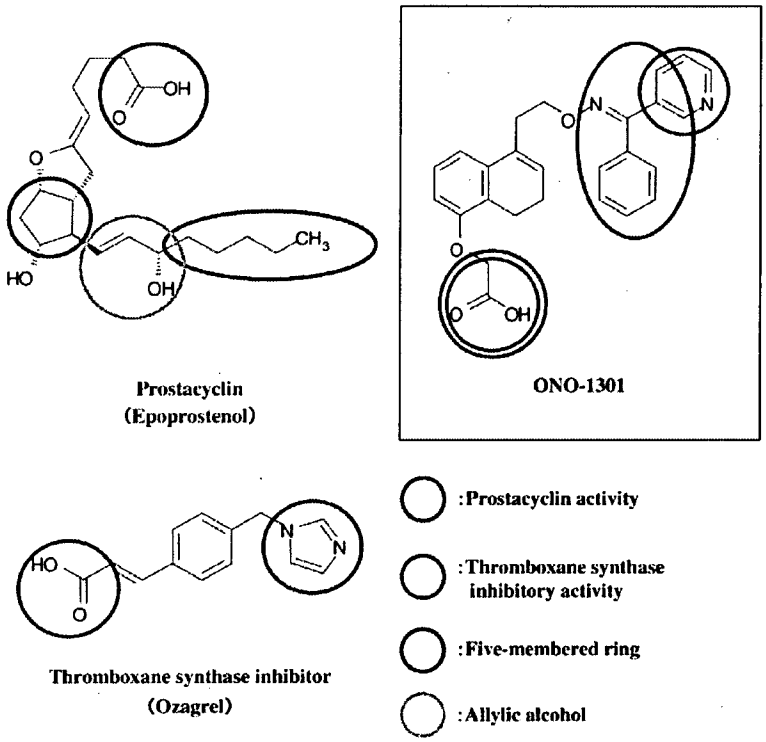

Figure 1. Chemical structures of ONO-1301, epoprostenol (prostacyclin analog), and ozagrel (thromboxane synthase inhibitor). Epoprostenol shares common characteristics with prostanoid structures, including a five-membered ring and an allylic alcohol (*blue* and *yellow circles*, respectively). In contrast, ONO-1301 has a carboxylic acid and a lipid-soluble functional group that activates the prostacyclin receptor (*green circles*), but does not have prostanoid structures, which allow long-lasting prostacyclin activity. Unlike epoprostenol, ONO-1301 has thromboxane synthase inhibitory activity because of a 3-pyridine radical and carboxylic acid within its molecule (*red circles*), similar to ozagrel.

addition, ONO-1301 has a 3-pyridine radical, which is known to inhibit thromboxane synthase through interaction with carboxylic acid via a hydrogen bond (Figure 1). Repeated administration of ONO-1301 attenuated monocrotaline (MCT)-induced pulmonary hypertension and improved survival in rats. Although the half-life of plasma ONO-1301 concentration is longer than that of any other prostacyclin analogs, ONO-1301 still needs to be administered twice a day subcutaneously to achieve a significant improvement in pulmonary hypertension. For patients with pulmonary hypertension, development of a long-acting, sustained-release prostacyclin analog would be beneficial in terms of stable hemodynamics and quality of life. To overcome these problems, we developed a new drug delivery system for prostacyclin. We prepared a novel sustained-release prostacyclin analog polymerized with poly(D,L-lactic-co-glycolic acid) (PLGA) microspheres (ONO-1301MS). PLGA microspheres, which are biodegradable and biocompatible compounds, have been used as a controlled delivery system for proteins and drugs (15–20). The release of drug from PLGA microspheres occurs through degradation of the polymeric matrix. Here, we showed that a single subcutaneous administration of ONO-1301MS achieved sustained elevation of its circulating level for 3 weeks.

Thus, the purposes of this study were as follows: (*1*) to investigate whether a single subcutaneous administration of ONO-1301MS attenuates MCT-induced pulmonary hypertension in rats and (*2*) to elucidate the underlying mechanisms responsible for the beneficial effects of this compound.

METHODS

Preparation of ONO-1301MS

ONO-1301MS is polymerized ONO-1301 with PLGA microspheres. ONO-1301 and PLGA (polylactic acid to glycolic acid ratio of 50:50) were dissolved in dichloromethane. The dissolved polymer was added to polyvinyl alcohol aqueous solution to form an oil-in-water emulsion. Then, dichloromethane was evaporated by stirring. After centrifugation and washing, ONO-1301MS was isolated by lyophilization.

Morphologic Studies by Scanning Electron Microscopy

To evaluate the shape and surface morphology of ONO-1301MS, we used a scanning electron microscope (model S-2460N; Hitachi, Tokyo, Japan). After lyophilization, the microspheres were mounted on an aluminum stub and coated with a thin layer (200 Å) of gold by an ion sputter (model E-1010; Hitachi). The surface morphology of the microsphere samples was then visualized under a scanning electron microscope.

Particle Diameter

ONO-1301MS was suspended in distilled water and dispersed by sonication. The particle diameter was measured by a laser diffraction particle size analyzer (model SALD-2100; Shimadzu, Kyoto, Japan).

Encapsulation Efficiency

Acetonitrile containing n-propyl 4-hydroxybenzoate served as an internal control to obtain the encapsulation efficiency, and this solution was homogenized by a sonicator. The concentration of ONO-1301 in this solution was analyzed by high-performance liquid chromatography (HPLC). The encapsulation efficiency was calculated as follows:

$$\text{Encapsulation efficiency}(\%) = (\text{measured value}/\text{theoretical value}) \times 100.$$

In Vitro Release of ONO-1301 from PLGA Microspheres

ONO-1301MS was suspended in phosphate-buffered saline (0.067 mol/L salt concentration, pH 6.8) containing 0.2% Tween-80 to adjust the concentration of ONO-1301 to 100 μg/ml. This solution was aliquoted into 1 ml and incubated at 37°C. At various time intervals, one of the aliquots was centrifuged for 5 minutes at 12,000 rpm. The supernatant was discarded, the pellet was dissolved in acetonitrile, and the remaining amount of ONO-1301 was analyzed by HPLC.

Animal Models

We used 5-week-old male Wistar rats weighing 95 to 110 g. The rats were randomly given a subcutaneous injection of either 60 mg/kg MCT or 0.9% saline, and assigned to receive a subcutaneous injection of 100 mg/kg ONO-1301MS or 0.9% saline. This protocol resulted in the creation of three groups: normal rats given 0.9% saline (sham group, n = 10), MCT rats given 0.9% saline (control group, n = 11), and MCT rats treated with ONO-1301 MS (treated group, n = 11). We chose the maximum dose that did not induce significant hypotension (*see* Figure E1 in the online supplement).

In Vivo Experimental Protocol

After anesthetization by an intraperitoneal injection of 30 mg/kg pentobarbital, rats were given a subcutaneous injection of either 60 mg/kg MCT or 0.9% saline. Subsequently, rats received a single subcutaneous injection of 100 mg/kg ONO-1301MS or 0.9% saline. ONO-1301MS was suspended with 0.9% saline containing 0.2% Tween-80. Hemodynamic measurements and histologic analyses were performed on Day 21. For hemodynamic measurements, rats were anesthetized by intraperitoneal injection of 20 mg/kg pentobarbital, and the following indexes were recorded after an equilibration period. A polyethylene catheter (model PE-50; BD Biosciences, San Jose, CA) was inserted into the right carotid artery to measure heart rate and mean arterial pressure. The catheter was inserted through the right jugular vein into the right ventricle for the measurement of RV pressure. The values of heart rate, mean arterial pressure, and systolic RV pressure were calculated from a series of 20 consecutive heart beats in each rat. Finally, cardiac arrest was induced by injection of 2 mmol/L potassium chloride through the catheter. The ventricles and lungs were excised, dissected free, and weighed. The RV weight to body weight ratio (RV/BW), left ventricular plus septal weight to body weight ratio (LV + S/BW), and RV weight to left ventricular plus septal weight ratio (RV/LV + S) were calculated as indexes of ventricular hypertrophy, as reported previously (21). All protocols were performed in accordance with the guidelines of the Animal Care Ethics Committee of the National Cardiovascular Center Research Institute (Osaka, Japan).

Morphometric Analysis of Pulmonary Arteries

Paraffin sections of 4-μm thickness were obtained from the lower region of the right lung and stained with hematoxylin and eosin. Analysis of the medial wall thickness of the pulmonary arteries was performed as described previously (22). In brief, the external diameter and the medial wall thickness were measured in 20 muscular arteries (25–100-μm external diameter) per lung section. For each artery, the medial wall thickness was expressed as follows:

$$\%\,\text{wall thickness} = ([\text{medial thickness} \times 2]/\text{external diameter}) \times 100$$

A lung section was obtained from individual rats for comparison among the three groups (n = 5 in each group).

Assay of Plasma Levels of ONO-1301 and Cyclic AMP

To investigate whether a single subcutaneous administration of ONO-1301MS produces long-lasting prostacyclin activity in rats, we measured plasma levels of ONO-1301 and cyclic AMP (cAMP) after ONO-1301MS injection. Fourteen rats were assigned to receive a single subcutaneous injection of 100 mg/kg ONO-1301MS or 0.9% saline (n = 7 in each group), and blood was drawn from the tail vein on Days 0, 7, 14, and 21. Blood was immediately transferred to a chilled glass tube containing 1 mg/ml disodium ethylenediaminetetraacetic acid and 500 U/ml aprotinin, and centrifuged immediately. Plasma ONO-1301 level was measured by liquid chromatography tandem mass spectrometry assay. Plasma cAMP level was measured with a radioimmunoassay kit (cAMP assay kit; Yamasa Co., Chiba, Japan), as reported previously (23).

Assay of Urinary Level of 11-Dehydro Thromboxane B_2

To investigate the effect of ONO-1301MS on thromboxane synthesis in rats, we measured urinary level of 11-dehydro thromboxane B_2 (11-$DTXB_2$), a metabolite of thromboxane A_2 (TXA_2), after single subcutaneous injection of ONO-1301MS (100 mg/kg) or vehicle (n = 8 in each group). Urine samples were collected for 24 hours on Day 14 by using metabolic cages, and urinary concentration of 11-$DTXB_2$ was measured with an enzyme immunoassay kit (11-$DTXB_2$ assay kit; Cayman Chemical Co., Ann Arbor, MI). The urinary level of 11-$DTXB_2$ was expressed as the ratio of urinary 11-$DTXB_2$ concentration to that of creatinine, as reported previously (24).

Western Blot Analysis

To investigate the effect of ONO-1301MS on proliferative signaling pathways in homogenized lung tissue, the protein expression of extracellular signal-regulated protein kinase (ERK) 1/2 and phospho-ERK1/2 was determined by Western blotting. Western blotting was performed using rabbit monoclonal antibodies raised against ERK1/2 and phospho-ERK1/2 (Cell Signaling Technology, Danvers, MA). Peripheral samples of lung tissue were obtained on Day 21 from individual rats for comparison among the three groups (n = 6 in each group). Positive protein bands were visualized by means of chemiluminescence (enhanced chemiluminescence kit; Amersham Biosciences, Little Chalfont, UK). Western blot analysis using a mouse polyclonal antibody raised against β-actin (Sigma Chemical Corp., St. Louis, MO) was used as a protein loading control. The resultant bands were quantified using Image J 1.36 imaging software (National Institutes of Health; http://rsb.info.nih.gov/ij/).

Statistical Analysis

All data were expressed as mean ± SEM. Comparisons of parameters among the three groups were made by one-way analysis of variance (ANOVA), followed by Newman-Keuls test. Comparisons of the time course of parameters between the two groups were made by two-way ANOVA for repeated measures, followed by Newman-Keuls test. A value of $P < 0.05$ was considered statistically significant.

RESULTS

Characterization of ONO-1301MS

We prepared three kinds of ONO-1301MS (samples 1, 2, and 3). The external surface morphology of ONO-1301MS (sample 2 as a representative sample) exhibited a spherical shape with a smooth and uniform surface (Figure 2A). The particle size in samples 1, 2, and 3 was 21.2, 42.0, and 71.1 μm, respectively (Figure 2B; sample 2 as a representative sample). Encapsulation efficiency in each sample was 5.1, 21.8, and 17.4%, respectively. *In vitro*, each sample had different time periods of ONO-1301 release at 2, 3, and 4 weeks, respectively (Figure 2C). These data suggest that we were able to vary the release period of ONO-1301.

Long-lasting Activity of ONO-1301MS

To investigate the pharmacokinetics *in vivo*, we measured plasma ONO-1301 level after a single subcutaneous administration of ONO-1301MS, which was designed to release ONO-1301 for 3 weeks (sample 2). ONO-1301 was detected in plasma for 3 weeks, whereas plasma ONO-1301 level at baseline in the ONO-1301MS group and at all times in the vehicle group was below the detection limit (Figure 3A). In addition, plasma cAMP level after a single subcutaneous administration of ONO-1301MS was significantly higher than that in the control group (Figure 3B). Interestingly, the increase in plasma cAMP level lasted for over 2 weeks in parallel with the change in plasma ONO-1301MS level (Figure 3). These results suggest that subcutaneous administration of ONO-1301MS achieves long-lasting activity in rats.

Inhibitory Effect of ONO-1301MS on Thromboxane Synthase

Urinary level of 11-$DTXB_2$ was markedly elevated 14 days after MCT injection (Figure 4). However, treatment with ONO-1301MS significantly decreased urinary level of 11-$DTXB_2$ in MCT rats. These results suggest that ONO-1301MS has a sustained inhibitory effect on thromboxane synthase activity.

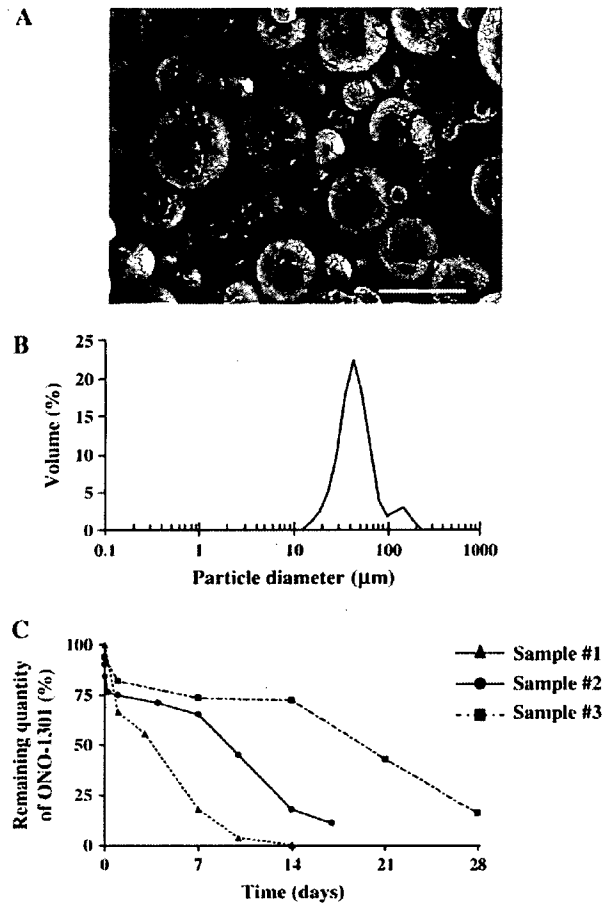

Figure 2. Physicochemical characteristics and *in vitro* release of ONO-1301. (*A*) Morphology of ONO-1301MS (sample 2) studied by scanning electron microscopy. *Scale bar* = 50 μm. (*B*) Particle diameter of ONO-1301MS (sample 2) obtained by a laser diffraction particle size analyzer. (*C*) Release profiles of ONO-1301MS in each sample.

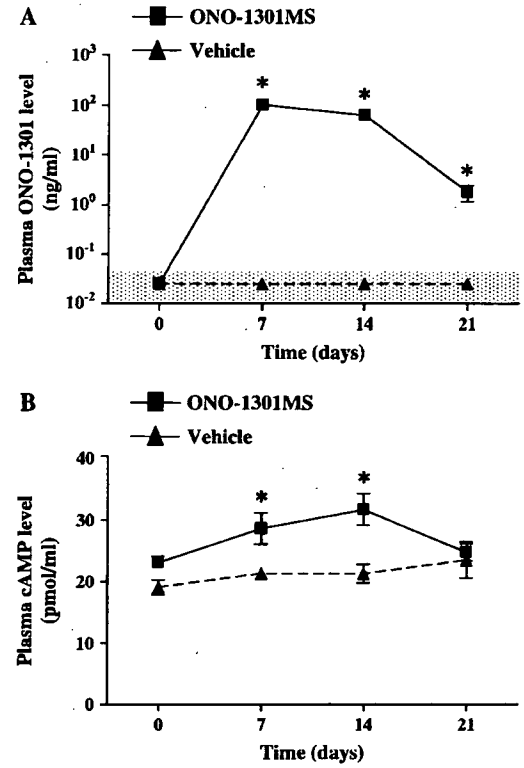

Figure 3. Time course changes in plasma ONO-1301 and cAMP. (*A*) Plasma ONO-1301 concentration after a single subcutaneous administration of ONO-1301MS or vehicle. The *shaded area* indicates below the lower limit of quantification (0.025 ng/ml) and is treated as 0 in the statistical analysis. (*B*) Changes in plasma cAMP level after a single subcutaneous administration of ONO-1301 MS or vehicle. Data are mean ± SEM. $*P < 0.05$ versus vehicle.

Effects of ONO-1301MS on Pulmonary Hemodynamics and Vascular Remodeling

Three weeks after MCT injection, RV systolic pressure was markedly increased (Figure 5). However, the increase in RV systolic pressure was significantly attenuated in the treated group. Similarly, the increases in RV/BW and RV/LV + S in MCT rats were significantly attenuated by treatment with ONO-1301MS (Figure 5). There were no significant differences in heart rate or mean arterial pressure among the three groups (Table 1). Histologic examination demonstrated that hypertrophy of the pulmonary vascular wall was attenuated in the treated group compared with that in the control group (Figure 6).

No adverse reactions, such as flushing, diarrhea, or hypotension, were observed in the treated group, and there were no significant differences in blood biochemical markers of liver and renal function among the three groups (mean value ± SEM in sham, control, and treated group were, respectively: 139 ± 14, 145 ± 20, and 102 ± 12 IU/L in aspartate aminotransferase; 53 ± 3, 54 ± 5, and 45 ± 3 IU/L in alanine aminotransferase; 0.1 ± 0, 0.1 ± 0, and 0.1 ± 0 mg/dl in total bilirubin; 16.2 ± 1.1, 16.2 ± 0.4, and 15.4 ± 1.2 mg/dl in urea nitrogen; 0.22 ± 0.01, 0.21 ± 0.01, and 0.21 ± 0.01 mg/dl in creatinine; n = 5 in each group.). Moreover, no abnormality was observed at the injection site.

Inhibitory Effect of ONO1301-MS on Proliferative Signals

To investigate the effect of ONO1301-MS on proliferative signals in the lung, Western blot analyses were performed. There were no significant differences in the expression of ERK1 and ERK2 among the three groups (Figure 7). However, phosphorylation of ERK1 and ERK2 was significantly increased in the control group, whereas these increases were markedly attenuated in the treatment group (Figure 7).

DISCUSSION

In the present study, we demonstrated that (*1*) a novel sustained-release prostacyclin analog polymerized with PLGA

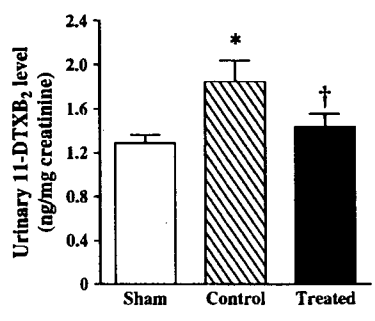

Figure 4. Effect of ONO-1301MS on thromboxane synthesis. Changes in urinary 11-dehydro thromboxane B_2 (11-DTXB_2) level on Day 14. Sham = sham rats given vehicle; control = monocrotaline (MCT)-treated rats given vehicle; treated = MCT rats treated with ONO-1301MS. Data are mean ± SEM. $*P < 0.05$ versus sham; $^{\dagger}P < 0.05$ versus control.

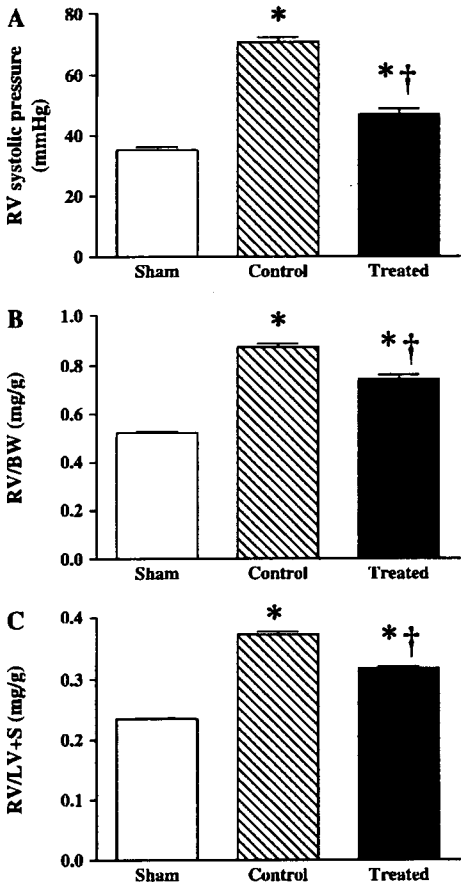

Figure 5. Effects of ONO-1301MS on pulmonary hemodynamics. (*A*) Effects of ONO-1301MS on right ventricular (RV) systolic pressure, (*B*) RV weight to body weight (RV/BW), and (C) RV weight to left ventricular plus septal weight (RV/LV + S). Sham = sham rats given vehicle; control = monocrotaline (MCT)-treated rats given vehicle; treated = MCT rats treated with ONO-1301MS. Data are mean ± SEM. $^*P < 0.05$ versus sham; $^\dagger P < 0.05$ versus control.

microspheres (ONO-1301MS) allowed a 3-week elevation of its circulating level, (*2*) ONO-1301MS had a sustained inhibitory effect on thromboxane synthase activity, and (*3*) a single subcutaneous administration of ONO-1301MS attenuated MCT-induced pulmonary hypertension in rats.

TABLE 1. PHYSIOLOGIC PROFILES OF THREE EXPERIMENTAL GROUPS

	Sham*	Control†	Treated‡
No. of rats	10	11	11
BW, g	203 ± 4	165 ± 7§	175 ± 3§
Heart rate, beats/min	454 ± 7	441 ± 10	445 ± 6
Mean arterial pressure, mm Hg	110 ± 2	111 ± 3	107 ± 2
LV + S/BW, mg/g	2.23 ± 0.02	2.34 ± 0.02§	2.34 ± 0.04§

Definition of abbreviations: BW = body weight; LV = left ventricle; LV + S/BW = LV plus septal weight to body weight ratio.

Data are mean ± SEM. These measurements were performed on Day 21.

* Sham = rats given vehicle.

† Control = MCT rats given vehicle.

‡ Treated = MCT rats treated with ONO-1301MS.

§ $P < 0.05$ versus sham.

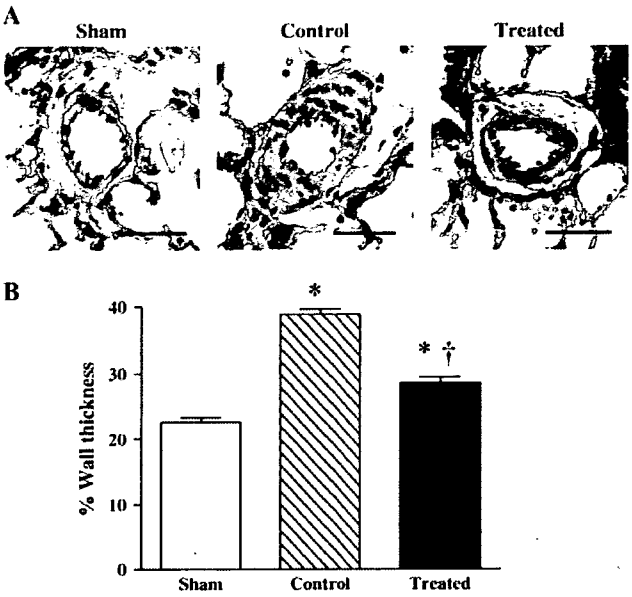

Figure 6. Effect of ONO-1301MS on vascular remodeling. (*A*) Representative photomicrographs of peripheral pulmonary arteries on Day 21. *Scale bars* = 50 μm. (*B*) Quantitative analysis of percentage of wall thickness in peripheral pulmonary arteries. Data are mean ± SEM. $^*P < 0.05$ versus sham; $^\dagger P < 0.05$ versus control.

Conventional prostacyclin and its analogs need continuous infusion or frequent administration because of their short duration of action. Previously, we reported a new type of prostacyclin agonist, ONO-1301, which has long-lasting prostacyclin activity and an inhibitory effect on thromboxane synthase (14). Although ONO-1301 has such interesting features, it still needs to be administered twice a day to achieve a significant improvement in pulmonary hypertension. To overcome this problem, we developed a new drug delivery system for prostacyclin. We polymerized ONO-1301 with PLGA microspheres to develop a novel sustained-release prostacyclin analog.

PLGA microspheres have been used as a controlled delivery system for bioactive agents (25). The release of bioactive agents from PLGA microspheres occurs through hydrolytic degradation of the polymeric matrix. Importantly, PLGA has already been used in humans. PLGA microspheres containing leuprorelin, a potent luteinizing hormone–releasing hormone analog, have been administered to patients with prostate and breast cancer by subcutaneous injection (26, 27). The rate of release of contents of PLGA microspheres can be changed by varying the factors affecting the hydrolytic degradation behavior of PLGA, such as lactate acid to glycolic acid ratio, average molecular weight of PLGA, and particle size (25). In the present study, we could control the degradation rate of ONO-1301MS. ONO-1301MS was designed to release ONO-1301 for 3 weeks, because it takes 3 weeks to induce pulmonary hypertension in rats after MCT injection. The present study demonstrated that the contained ONO-1301 was released for 3 weeks *in vitro*, producing a 3-week elevation of its circulating level after a single administration *in vivo*. It should be noted that only a single subcutaneous administration of ONO-1301MS attenuated MCT-induced pulmonary hypertension in rats. Thus, it might be possible to extend the administration interval for ONO-1301MS considerably longer than that with current prostacyclin analogs, and this could improve the quality of life in patients with pulmonary hypertension.

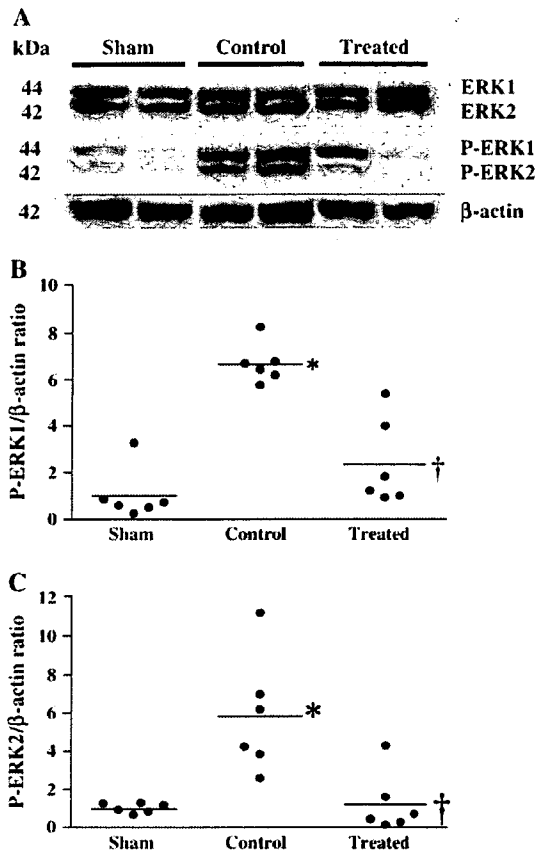

Figure 7. Effect of ONO-1301MS on extracellular signal-regulated protein kinase (ERK) phosphorylation. (*A*) Representative Western blotting for ERK, phospho-ERK (P-ERK) and β-actin (protein loading control) in lungs on Day 21 (n = 6 in each group). (*B* and *C*) Scatter plot of quantitative analysis of P-ERK expression in lung tissue. *Horizontal lines* in this figure show the mean value. $^{*}P < 0.05$ versus sham; $^{\dagger}P < 0.05$ versus control.

With regard to cAMP, which is a second messenger of prostacyclin and its analogs, it has been reported that plasma cAMP level remained increased after administration of prostacyclin analogs (23, 28). In our results, administration of ONO-1301MS increased the plasma cAMP level for over 2 weeks. This increase in plasma cAMP level was parallel to the change in plasma ONO-1301 level. In addition, ONO-1301MS attenuated the increase in urinary 11-$DTXB_2$ level in MCT rats 14 days after single administration. These results support that a single administration of ONO-1301MS produced a sustained beneficial effect for 3 weeks.

In the present study, we chose the maximum dose that did not induce significant hypotension. We did dose–response studies using ONO-1301MS (30, 100, and 300 mg/kg, respectively) (*see* Figure E1). ONO-1301MS at 300 mg/kg has induced significant hypotension. In addition, ONO-1301MS at 30 mg/kg did not significantly decrease RV systolic pressure (*see* Figure E3). On the other hand, ONO-1301MS at 100 mg/kg significantly decreased RV systolic pressure without significant hypotension. Furthermore, a single injection of 100 mg/kg ONO-1301 without PLGA or PLGA without ONO-1301 to MCT rats did not influence hemodynamics and vascular remodeling (*see* Figures E1–E3). These results suggest that a single injection of ONO-1301MS ameliorates MCT-induced pulmonary hypertension. Consistent with these hemodynamic data, RV/BW and medial wall thickness of pulmonary arteries, as indexes of RV hypertrophy and elevation of pulmonary arteriolar resistance, respectively, were significantly attenuated by the treatment with ONO-1301MS.

In histologic analysis, hypertrophy of pulmonary vessels after MCT injection was significantly attenuated by treatment with ONO-1301MS. An earlier clinical trial has shown that long-term therapy with epoprostenol significantly reduces pulmonary vascular resistance in patients who have no short-term response to vasodilators (5). It is speculated that such a beneficial effect of epoprostenol is caused not only by vasodilatation and antiplatelet aggregation but also by an antiproliferative effect on SMCs and reverse remodeling of pulmonary arteries. In the present study, phosphorylated ERK1/2 in the lung tissue was significantly increased after MCT injection. However, this increase was markedly attenuated by treatment with ONO-1301MS. ERK is the final component of the mitogen-activated protein kinase cascade. Prostacyclin has been shown to inhibit phosphorylation of ERK1/2 through the activation of cAMP (29). With respect to this signaling, protein kinase A (PKA), an intracellular effector of cAMP, has been shown to negatively regulate the Ras–ERK cascade by phosphorylating Raf and by preventing its association with active Ras (30). Furthermore, we previously reported that ONO-1301 inhibited pulmonary fibroblast proliferation through activation of the cAMP/PKA pathway (31). Therefore, it is interesting to speculate that ONO-1301MS may have antiproliferative effects on pulmonary vascular SMCs at least in part through inhibition of ERK via a cAMP-dependent pathway, although the precise mechanism remains to be elucidated.

ONO-1301MS significantly decreased urinary level of 11-$DTXB_2$, a metabolite of TXA_2. TXA_2 is a vasoconstrictor and a potent stimulator of platelet aggregation (32, 33). Moreover, it has been demonstrated that TXA_2 induces mitosis in vascular SMCs through activation of ERK (34, 35). It has been suggested that imbalance of thromboxane and prostacyclin plays an important role in the development of pulmonary hypertension (36). Previous reports showed that administration of thromboxane synthase inhibitor modestly attenuated pulmonary hypertension (37, 38). Thus, an inhibitory effect of ONO-1301MS on thromboxane synthase may also contribute to improvement in pulmonary hypertension.

In the present study, no adverse reactions, such as flushing, diarrhea, hypotension, renal dysfunction, or hepatic dysfunction, were observed in the treated group. However, further preclinical studies are necessary to confirm the safety and efficacy of ONO-1301MS before clinical trials start in patients with pulmonary arterial hypertension.

We did not measure cardiac output because of technical and mechanical problems. To support our hemodynamic data, we evaluated a variety of indexes, such as RV/BW and medial wall thickness of pulmonary arteries. These physiologic and histologic findings have been consistent with data on RV systolic pressure. Therefore, it is unlikely that the reduction in RV systolic pressure observed in the present study was related to the reduced cardiac output.

In conclusion, we developed a novel sustained-release prostacyclin analog polymerized with PLGA microspheres (ONO-1301MS), which achieved a 3-week elevation of its circulating level and simultaneously increased plasma cAMP levels for over 2 weeks, and had an inhibitory effect on thromboxane synthase. A single subcutaneous administration of ONO-1301MS attenuated MCT-induced pulmonary hypertension in rats. ONO-1301MS may have an antiproliferative effect through inhibition of ERK phosphorylation. This drug delivery system for a prostacyclin analog may be a new therapeutic strategy for the treatment of pulmonary arterial hypertension.

Conflict of Interest Statement: None of the authors has a financial relationship with a commercial entity that has an interest in the subject of this manuscript.

References

1. McLaughlin VV, McGoon MD. Pulmonary arterial hypertension. *Circulation* 2006;114:1417–1431.
2. Moncada S, Gryglewski R, Bunting S, Vane JR. An enzyme isolated from arteries transforms prostaglandin endoperoxides to an unstable substance that inhibits platelet aggregation. *Nature* 1976;263:663–665.
3. Moncada S, Vane JR. Arachidonic acid metabolites and the interactions between platelets and blood-vessel walls. *N Engl J Med* 1979;300: 1142–1147.
4. Humbert M, Sitbon O, Simonneau G. Treatment of pulmonary arterial hypertension. *N Engl J Med* 2004;351:1425–1436.
5. McLaughlin VV, Genthner DE, Panella MM, Rich S. Reduction in pulmonary vascular resistance with long-term epoprostenol (prostacyclin) therapy in primary pulmonary hypertension. *N Engl J Med* 1998;338:273–277.
6. McLaughlin VV, Shillington A, Rich S. Survival in primary pulmonary hypertension: the impact of epoprostenol therapy. *Circulation* 2002; 106:1477–1482.
7. Sitbon O, Humbert M, Nunes H, Parent F, Garcia G, Herve P, Rainisio M, Simonneau G. Long-term intravenous epoprostenol infusion in primary pulmonary hypertension: prognostic factors and survival. *J Am Coll Cardiol* 2002;40:780–788.
8. Okano Y, Yoshioka T, Shimouchi A, Satoh T, Kunieda T. Orally active prostacyclin analogue in primary pulmonary hypertension. *Lancet* 1997;349:1365.
9. Nagaya N, Uematsu M, Okano Y, Satoh T, Kyotani S, Sakamaki F, Nakanishi N, Miyatake K, Kunieda T. Effect of orally active prostacyclin analogue on survival of outpatients with primary pulmonary hypertension. *J Am Coll Cardiol* 1999;34:1188–1192.
10. Olschewski H, Simonneau G, Galie N, Higenbottam T, Naeije R, Rubin LJ, Nikkho S, Speich R, Hoeper MM, Behr J, *et al.* Inhaled iloprost for severe pulmonary hypertension. *N Engl J Med* 2002;347:322–329.
11. Simonneau G, Barst RJ, Galie N, Naeije R, Rich S, Bourge RC, Keogh A, Oudiz R, Frost A, Blackburn SD, *et al.* Continuous subcutaneous infusion of treprostinil, a prostacyclin analogue, in patients with pulmonary arterial hypertension: a double-blind, randomized, placebo-controlled trial. *Am J Respir Crit Care Med* 2002;165:800–804.
12. Badesch DB, McLaughlin VV, Delcroix M, Vizza CD, Olschewski H, Sitbon O, Barst RJ. Prostanoid therapy for pulmonary arterial hypertension. *J Am Coll Cardiol* 2004;43:56S–61S.
13. Laliberte K, Arneson C, Jeffs R, Hunt T, Wade M. Pharmacokinetics and steady-state bioequivalence of treprostinil sodium (Remodulin) administered by the intravenous and subcutaneous route to normal volunteers. *J Cardiovasc Pharmacol* 2004;44:209–214.
14. Kataoka M, Nagaya N, Satoh T, Itoh T, Murakami S, Iwase T, Miyahara Y, Kyotani S, Sakai Y, Kangawa K, *et al.* A long-acting prostacyclin agonist with thromboxane inhibitory activity for pulmonary hypertension. *Am J Respir Crit Care Med* 2005;172:1575–1580.
15. Alonso MJ, Gupta RK, Min C, Siber GR, Langer R. Biodegradable microspheres as controlled-release tetanus toxoid delivery systems. *Vaccine* 1994;12:299–306.
16. Seagal J, Edry E, Keren Z, Leider N, Benny O, Machluf M, Melamed D. A fail-safe mechanism for negative selection of isotype-switched B cell precursors is regulated by the Fas/FasL pathway. *J Exp Med* 2003;198:1609–1619.
17. Mullerad J, Cohen S, Benharroch D, Apte RN. Local delivery of IL-1 alpha polymeric microspheres for the immunotherapy of an experimental fibrosarcoma. *Cancer Invest* 2003;21:720–728.
18. Mullerad J, Cohen S, Voronov E, Apte RN. Macrophage activation for the production of immunostimulatory cytokines by delivering interleukin 1 via biodegradable microspheres. *Cytokine* 2000;12:1683–1690.
19. Sanchez A, Gupta RK, Alonso MJ, Siber GR, Langer R. Pulsed controlled-released system for potential use in vaccine delivery. *J Pharm Sci* 1996;85:547–552.
20. Roullin VG, Lemaire L, Venier-Julienne MC, Faisant N, Franconi F, Benoit JP. Release kinetics of 5-fluorouracil-loaded microspheres on an experimental rat glioma. *Anticancer Res* 2003;23:21–25.
21. Kimura H, Kasahara Y, Kurosu K, Sugito K, Takiguchi Y, Terai M, Mikata A, Natsume M, Mukaida N, Matsushima K, *et al.* Alleviation of monocrotaline-induced pulmonary hypertension by antibodies to monocyte chemotactic and activating factor/monocyte chemoattractant protein-1. *Lab Invest* 1998;78:571–581.
22. Ono S, Voelkel NF. PAF antagonists inhibit monocrotaline-induced lung injury and pulmonary hypertension. *J Appl Physiol* 1991;71:2483–2492.
23. Itoh T, Nagaya N, Fujii T, Iwase T, Nakanishi N, Hamada K, Kangawa K, Kimura H. A combination of oral sildenafil and beraprost ameliorates pulmonary hypertension in rats. *Am J Respir Crit Care Med* 2004;169:34–38.
24. Fiorucci S, Mencarelli A, Meneguzzi A, Lechi A, Morelli A, del Soldato P, Minuz P. NCX-4016 (NO-aspirin) inhibits lipopolysaccharide-induced tissue factor expression in vivo: role of nitric oxide. *Circulation* 2002;106:3120–3125.
25. Shive MS, Anderson JM. Biodegradation and biocompatibility of PLA and PLGA microspheres. *Adv Drug Deliv Rev* 1997;28:5–24.
26. Fornara P, Jocham D. Clinical study results of the new formulation leuprorelin acetate three-month depot for the treatment of advanced prostate carcinoma. *Urol Int* 1996;56:18–22.
27. Schmid P, Untch M, Kosse V, Bondar G, Vassiljev L, Tarutinov V, Lehmann U, Maubach L, Meurer J, Wallwiener D, *et al.* Leuprorelin acetate every-3-months depot versus cyclophosphamide, methotrexate, and fluorouracil as adjuvant treatment in premenopausal patients with node-positive breast cancer: the TABLE study. *J Clin Oncol* 2007;25:2509–2515.
28. Beghetti M, Reber G, de Moerloose P, Vadas L, Chiappe A, Spahr-Schopfer I, Rimensberger PC. Aerosolized iloprost induces a mild but sustained inhibition of platelet aggregation. *Eur Respir J* 2002; 19:518–524.
29. Li RC, Cindrova-Davies T, Skepper JN, Sellers LA. Prostacyclin induces apoptosis of vascular smooth muscle cells by a cAMP-mediated inhibition of extracellular signal-regulated kinase activity and can counteract the mitogenic activity of endothelin-1 or basic fibroblast growth factor. *Circ Res* 2004;94:759–767.
30. Cook SJ, McCormick F. Inhibition by cAMP of Ras-dependent activation of Raf. *Science* 1993;262:1069–1072.
31. Murakami S, Nagaya N, Itoh T, Kataoka M, Iwase T, Horio T, Miyahara Y, Sakai Y, Kangawa K, Kimura H. Prostacyclin agonist with thromboxane synthase inhibitory activity (ONO-1301) attenuates bleomycin-induced pulmonary fibrosis in mice. *Am J Physiol Lung Cell Mol Physiol* 2006;290:L59–L65.
32. Hamberg M, Svensson J, Samuelsson B. Prostaglandin endoperoxides: a new concept concerning the mode of action and release of prostaglandins. *Proc Natl Acad Sci USA* 1974;71:3824–3828.
33. Svenssen J, Strandberg K, Tuvemo T, Hamberg M. Thromboxane A2: effects on airway and vascular smooth muscle. *Prostaglandins* 1977; 14:425–436.
34. Sachinidis A, Flesch M, Ko Y, Schror K, Bohm M, Dusing R, Vetter H. Thromboxane A2 and vascular smooth muscle cell proliferation. *Hypertension* 1995;26:771–780.
35. Morinelli TA, Tempel GE, Jaffa AA, Silva RH, Naka M, Folger W, Halushka PV. Thromboxane A2/prostaglandin H2 receptors in streptozotocin-induced diabetes: effects of insulin therapy in the rat. *Prostaglandins* 1993;45:427–438.
36. Christman BW, McPherson CD, Newman JH, King GA, Bernard GR, Groves BM, Loyd JE. An imbalance between the excretion of thromboxane and prostacyclin metabolites in pulmonary hypertension. *N Engl J Med* 1992;327:70–75.
37. Nagata T, Uehara Y, Hara K, Igarashi K, Hazama H, Hisada T, Kimura K, Goto A, Omata M. Thromboxane inhibition and monocrotaline-induced pulmonary hypertension in rats. *Respirology* 1997;2:283–289.
38. Rich S, Hart K, Kieras K, Brundage BH. Thromboxane synthetase inhibition in primary pulmonary hypertension. *Chest* 1987;91:356–360.

A reprint from
OPTICAL ENGINEERING ISSN 0091-3286

Intense clean characteristic flash x-ray irradiation from an evaporating molybdenum diode

Michiaki Sagae
Eiichi Sato
Etsuro Tanaka
Hidezo Mori
Toshiaki Kawai
Takashi Inoue
Akira Ogawa
Shigehiro Sato
Kazuyoshi Takayama
Jun Onagawa
Hideaki Ido

Optical Engineering 46(2), 026502 (February 2007)

P.O. Box 10, Bellingham, Washington 98227 USA. Telephone 360/676-3290

Intense clean characteristic flash x-ray irradiation from an evaporating molybdenum diode

Michiaki Sagae
Eiichi Sato, MEMBER SPIE
Iwate Medical University
Department of Physics
3-16-1 Honchodori
Morioka 020-0015, Japan
E-mail: msagae@iwate-med.ac.jp

Etsuro Tanaka
Tokyo University of Agriculture
Department of Nutritional Science
Faculty of Applied Bioscience
1-1-1 Sakuragaoka
Setagaya-ku 156-8502, Japan

Hidezo Mori
National Cardiovascular Center Research Institute
Department of Cardiac Physiology
5-7-1 Fujishirodai, Suita
Osaka 565-8565, Japan

Toshiaki Kawai, MEMBER SPIE
Hamamatsu Photonics K. K.
Electron Tube Division 2
314-5 Shimokanzo
Iwata 438-0193, Japan

Takashi Inoue
Akira Ogawa
Iwate Medical University
Department of Neurosurgery
School of Medicine
19-1 Uchimaru
Morioka 020-8505, Japan

Shigehiro Sato
Iwate Medical University
Department of Microbiology
School of Medicine
19-1 Uchimaru
Morioka 020-8505, Japan

Kazuyoshi Takayama, MEMBER SPIE
Tohoku University
Shock Wave Research Center
Institute of Fluid Science
2-1-1 Katahira
Sendai 980-8577, Japan

Jun Onagawa
Hideaki Ido
Tohoku Gakuin University
Department of Applied Physics and Informatics
Faculty of Engineering
1-13-1 Chuo
Tagajo 985-8537, Japan

0091-3286/2007/$25.00 © 2007 SPIE

Abstract. In a flash x-ray generator, a 150-nF condenser is charged up to 80 kV by a power supply, and flash x-rays are produced by the discharge. The x-ray tube is a demountable diode, and the turbomolecular pump evacuates air from the tube with a pressure of approximately 1 mPa. Since the electric circuit of the high-voltage pulse generator employs a cable transmission line, the high-voltage pulse generator produces twice the potential of the condenser charging voltage. Because bremsstrahlung rays are not emitted in the opposite direction of that of electron trajectory, clean molybdenum K-series characteristic x-rays can be produced without using a filter. When the charging voltage is increased, the K-series characteristic x-ray intensities of molybdenum increase. The K lines are clean and intense, and hardly any bremsstrahlung rays are detected. The x-ray pulse widths are approximately 100 ns, and the time-integrated x-ray intensity has a value of approximately 500 μGy per pulse at 1.0 m from the x-ray source, with a charging voltage of 80 kV. *© 2007 Society of Photo-Optical Instrumentation Engineers.*
[DOI: 10.1117/1.2541668]

Subject terms: flash x-ray; energy-selective radiography; characteristic x-rays; quasi-monochromatic x-rays; bremsstrahlung x-ray distribution.

Paper 050104R received Feb. 7, 2005; revised manuscript received Jan. 10, 2006; accepted for publication Aug. 10, 2006; published online Mar. 2, 2007. This paper is a revision of a paper presented at the SPIE conference on 26th International Congress on High-Speed Photography and Photonics, Sep. 2004, Alexandria, Virginia. The paper presented there appears (unrefereed) in SPIE proceedings Vol. 5580.

1 Introduction

In recent years, there have been several investigations dealing with the production of monochromatic x-rays in radiology and cardiology. Particularly, monochromatic parallel beams using synchrotrons have been employed to perform enhanced K-edge angiography[1,2] and x-ray phase imaging.[3,4] In angiography, parallel beams with photon energies of approximately 35 keV have been employed, since these beams are absorbed effectively by an iodine-based contrast medium. Subsequently, in cases where phase imaging is employed, the spatial resolution can be improved, and the number of tissues that can be observed using x-rays increases.

We have developed several different soft flash x-ray generators[5–11] with photon energy of less than 150 keV corresponding to specific radiographic objectives, and a major goal in our research is the development of an intense and clean monochromatic x-ray generator that can impact applications with medical radiography. Recently, we have succeeded in producing intense K-series characteristic x-rays from the axial direction of linearly evaporating targets.[12–16] In metal vapor, bremsstrahlung spectra with photon energies of higher than the K-absorption edge are effectively absorbed and are converted into fluorescent x-rays. The vapor then transmits the fluorescent rays easily. However, the bremsstrahlung x-rays are produced using a molybdenum target,[12] since high-photon-energy bremsstrahlung x-rays are not absorbed effectively in the linear vapor.

To produce clean characteristic x-rays of molybdenum, silver, cerium, ytterbium, and tungsten, we have developed a compact and weak flash x-ray generator,[17] and succeeded in producing clean molybdenum K-series characteristic x-rays of approximately 1×10^7 photons/cm^2 at 1.0 m per pulse using the angle dependence of bremsstrahlung x-rays, since bremsstrahlung rays are not emitted in the opposite direction to that of electron trajectory. Therefore, the K photons should be maximized by increasing both the tube voltage and current, and monochromatic Kα rays are selected using a zirconium filter.[18] Furthermore, both the bremsstrahlung and characteristic x-rays are produced in a metal vapor, and the vapor transmits K-series characteristic x-rays easily. Thus, we are very interested in the x-ray characteristics of a diode with an evaporating target formed by increasing the electrostatic energy in a high-voltage condenser.

In this work, we developed a new flash x-ray generator utilizing a ring-cathode molybdenum diode, used to perform a preliminary experiment for generating intense and clean K-series characteristic x-rays from an evaporated molybdenum target tip utilizing the angular dependence of the bremsstrahlung x-ray distribution.

2 Generator

2.1 *High-Voltage Circuit*

Figure 1 shows a block diagram of an intense flash x-ray generator. The generator consists of the following essential components: a high-voltage power supply, a high-voltage condenser with a capacity of approximately 150 nF, an air gap switch, a turbomolecular pump, a thyratron pulse generator as a trigger device, and a flash x-ray tube. In this

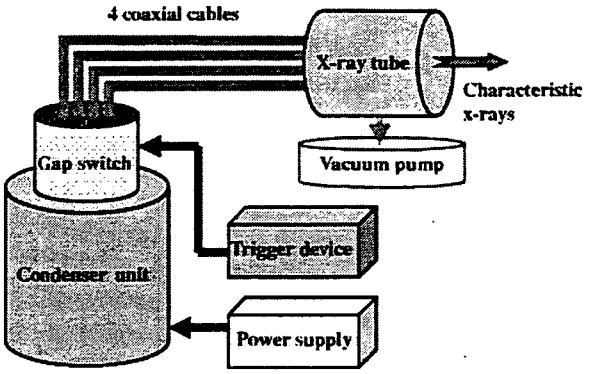

Fig. 1 Block diagram of the intense characteristic flash x-ray generator with a ring-cathode molybdenum diode.

generator, a four-cable transmission line is employed to increase maximum tube voltage using high-voltage reflection and to decrease the impedance of the generator. The high-voltage main condenser is charged up to 80 kV by the power supply, and electric charges in the condenser are discharged to the tube through the four cables after closing the gap switch with the trigger device (Fig. 2).

2.2 *X-Ray Tube*

The x-ray tube is a demountable cold-cathode diode that is connected to the turbomolecular pump with a pressure of approximately 1 mPa (Fig. 3). This tube consists of the following major parts: a ring-shaped graphite cathode with an inside diameter of 4.5 mm, a stainless-steel vacuum chamber, a nylon insulator, a polyethylene terephthalate (Mylar) x-ray window 0.25 mm in thickness, and a rod-shaped molybdenum target 3.0 mm in diameter. The distance between the target and cathode electrodes can be regulated from the outside of the tube, and is set to 1.5 mm. As electron beams from the cathode electrode are roughly converged to the target by the electric field in the tube, the vapor x-ray source forms at the solid target tip. Because bremsstrahlung rays are not emitted in the opposite direction to that of the electron trajectory (Fig. 4), clean molybdenum K-series characteristic x-rays can be produced without using a molybdenum filter.

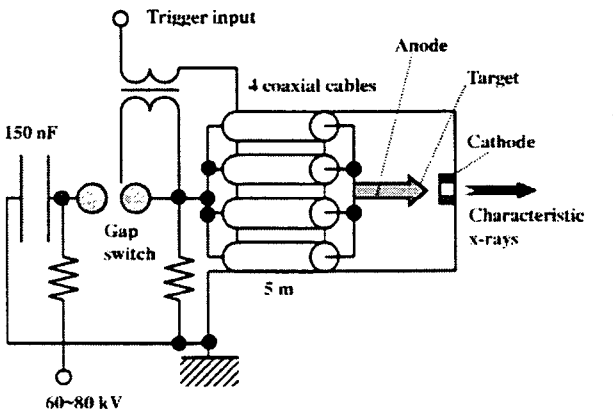

Fig. 2 Circuit diagram of the flash x-ray generator utilizing a coaxial transmission line.

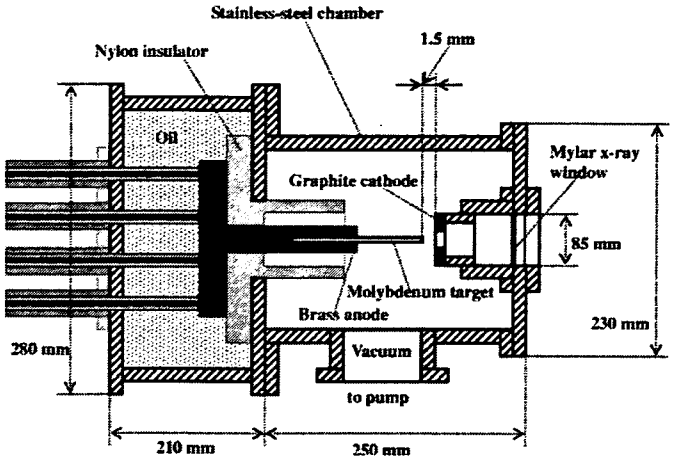

Fig. 3 Schematic drawing of the flash x-ray tube with a rod-shaped molybdenum target and a ring graphite cathode.

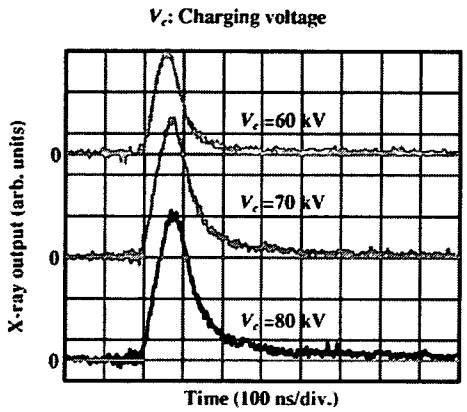

Fig. 5 X-ray outputs detected using a combination of a plastic scintillator and photomultiplier.

3 Characteristics

3.1 *Tube Voltage and Current*

In this generator, it was difficult to measure the tube voltage and current, since the tube voltages were high and there was no space to set a current transformer for measuring the tube current. The voltage and current roughly display damped oscillations. When the charging voltage is increased, both the maximum tube voltage and current increase. At a charging voltage of 80 kV, the estimated maximum values of the tube voltage and current are approximately 160 kV (two times the charging voltage) and 40 kA, respectively.

3.2 *X-Ray Output*

The x-ray output pulse was detected using a combination of a plastic scintillator and photomultiplier (Fig. 5). Due to photoelectric transfer characteristics, the pulse height was not proportional to the x-ray intensity. The x-ray pulse height increased with corresponding increases in the charging voltage. The x-ray pulse widths were approximately 100 ns, and the time-integrated x-ray intensity measured by a thermoluminescence dosimeter (Kyokko TLD Reader 1500 having MSO-S elements without energy compensation) had a value of approximately 500 μGy per pulse at 1.0 m from the x-ray source, with a charging voltage of 80 kV.

3.3 *X-Ray Source*

To observe the characteristic x-ray source, we employed a 100-μm-diam pinhole camera and an x-ray film (Polaroid XR-7) (Fig. 6). When the charging voltage was increased, both spot dimension and intensity increased. Because the maximum diameter was larger than the target diameter of 3.0 mm, the vapor x-ray source formed at the solid target tip.

3.4 *X-Ray Spectra*

X-ray spectra were measured by a transmission-type spectrometer with a lithium fluoride curved crystal 0.5 mm in thickness. The spectra were taken by a computed radiography (CR) system (Konica Regius 150)[19] with a wide dynamic range, and relative x-ray intensity was calculated from Dicom digital data. Using this spectrometer, it is easy to measure low intensity bremsstrahlung x-rays.[12,20] Figure

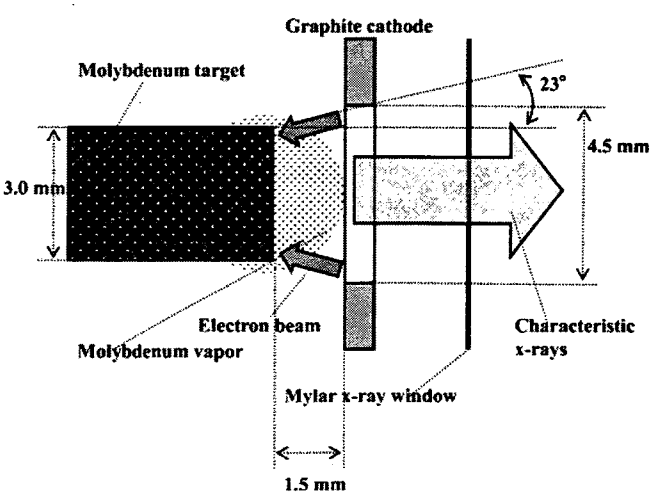

Fig. 4 Irradiation of characteristic x-rays using the angle dependence of bremsstrahlung x-ray intensity distribution. Bremsstrahlung rays are not emitted in the opposite direction of that of electron trajectory.

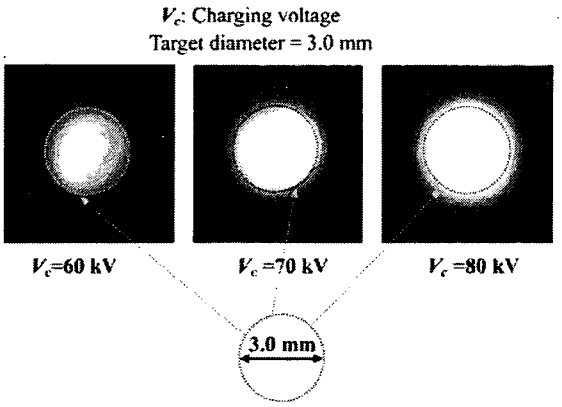

Fig. 6 Images of the characteristic x-ray source measured using a pinhole camera with changes in the charging voltage.